High-resolution late Middle Pleistocene paleoclimatic record from the Galería Complex, Atapuerca archaeological site, Spain - an environmental magnetic approach

Bógalo, M.F.[1*], Bradák, B.[1], Villalaín, J.J.[1], Calvo-Rathert, M.[1,2], González, M.I.[1], Heller, F.[3], Ortega, A.I.[4,5] and Parés, J.M.[4]

[1]Dpto. Física, Universidad de Burgos, Escuela Politécnica Superior, Avda. Cantabria s/n, 09006, Burgos, Spain. Email: mfbogalo@ubu.es, bradak.b@gmail.com, villa@ubu.es, mcalvo@ubu.es, miglez@ubu.es

[2]Hawaii Institute of Geophysics and Planetology, University of Hawaii at Manoa, Honolulu, HI, 86822, United States of America

[3]Institute of Geophysics, ETH Zürich, CH-8092 Zürich, Switzerland. Email: friedrich.heller@mag.ig.erdw.ethz.ch

[4]Centro Nacional sobre la Investigación Humana, Paseo Sierra de Atapuerca, s/n 09002, Burgos, Spain. Email: anaisabel.ortega@fa.cenieh.es, josep.pares@cenieh.es

[5]Fundación Atapuerca, Ctra. Logroño, 44, 09198 Ibeas de Juarros, Burgos, Spain. anaisabel.ortega60@gmail.com

*Corresponding author; email: mfbogalo@ubu.es

Abstract

The Galería Complex is a cave sediment succession at the Atapuerca paleoanthropological site (Burgos, Spain) that offers detailed environmental information about the late Middle Pleistocene, especially the period between marine oxygen isotope stages MIS10 and MIS7. Previous studies have reconstructed the chronology and detailed the environmental development of this key succession. We introduce rock magnetic climate proxies from the sedimentary units of the Galería succession that we correlate with the global climate record as represented by the marine oxygen isotope record. The cave sediment sequence consists of five infilling phases, four of which were sampled at high resolution across a 5 m thick composite profile. We propose a novel goethite climate proxy along with a frequently used ultrafine ferrimagnetic mineral proxy for paleoclimate reconstruction and detailed chronostratigraphic correlation with isotope stages and substages MIS10/MIS10-9, MIS9e-a and MIS8. The proxies reveal new paleoenvironmental information about paleoprecipitation and indicate that MIS9e was a humid (~650 mm/year maximum annual precipitation) and intense interglacial in northern Spain that declined in steps into the globally weak glacial stage MIS8. MIS8 consisted of drier periods with 430 to 510 mm/year annual precipitation and at least one humid substage (600 mm/year).

Keywords: Galería Complex; Atapuerca; Western Europe; late Middle Pleistocene; paleoclimatology; MIS9; MIS8; sediment mineralogy; environmental magnetism; goethite proxy.

Abbreviations[1]

[1] χ_{lf} - mass specific low field and low frequency magnetic susceptibility; χ_{fd} - frequency dependent susceptibility; χ_{hf} - mass specific high frequency magnetic susceptibility; SP - superparamagnetic; SD - single domain; MD - multidomain; ARM - anhysteretic remanent magnetization; χ_{ARM} - ARM susceptibility; IRM - isothermal remanent magnetization; SIRM - saturation isothermal remanent magnetization; AF - alternating field; $B_{1/2}$ or MDF - field at which half of the SIRM is reached or destroyed; DP - dispersion parameter; S - skewness; IRM_{RR} - IRM acquired and measured at 293 K (room temperature); IRM_{RL} - IRM acquired at 293 K (ca. 20°C) and measured at 77 K (ca. -196°C, liquid nitrogen temperature); IRM_{LL} - IRM acquired and measured at 77 K; SP_{LC} - absolute content of low coercivity superparamagnetic grains; $SP\%_{LC}$ - relative content of low coercivity superparamagnetic grains; G - absolute content of goethite; g% - relative content of goethite; SP_{HC} - absolute content of imperfect antiferromagnetic (e.g. goethite and hematite) SP grains; $SP\%_{HC}$ - relative content of imperfect antiferromagnetic SP grains; $H^{(b+d)}$-beam and diffuse solar irradiation; H(r) - reflected solar irradiation; MBB - Matuyama/Brunhes geomagnetic polarity reversal Boundary; MAP - mean annual precipitation; TT-OSL - thermally transferred optically stimulated luminescence; IRSL - infrared stimulated luminescence; pIR-IR - post-infrared IRSL; ESR - electron spin resonance.

1. Introduction

Cave sediments reflect environmental changes, document microenvironments, and register human activities (for inhabited caves). Cave infill consists of autochthonous and allochthonous sediments (Goldberg and Sherwood, 2006). Entrance facies are formed by allochthonous deposits that include fine-grained sediments transported from outside the cave by wind or water. Coarser clasts may be transported into the cave by slope processes. Interior facies include autochthonous sediments that can be classified as clastic or chemogenic deposits (i.e. speleothems), which often formed under vadose conditions. These clasts may consist of fluvial gravels and sands or deposits of laminated silts and clays often intercalated with speleothems. This facies could also contain colluvial material and clastic sediments from external environments, which can be frequently re-deposited and/or injected into the cave from long distances (e.g. Gillieson, 1998; Ford and Williams, 2007). Transportation and sedimentation of cave sediments are complex processes, although both the entrance and interior facies depend strongly on and reflect terrestrial climatic characteristics (e.g. Vallverdú i Poch, 2017).

The appearance and nature of human activity must also be considered in caves with multiple periods of human occupation, such as at the Sierra de Atapuerca archeological site. The Sierra de Atapuerca, located in Northern Spain (Fig. 1), provides a large amount of paleontological and archeological data documenting the first human appearance in Eurasia (e.g. Carbonell et al., 1995, 2008; Parés and Pérez-González, 1995; Arsuaga et al., 1997, 2014; Bermúdez de Castro et al., 1997) and has been added to UNESCO's World Heritage List in 2000. Excavated since 1976, various Atapuerca cave sites have provided a vast amount of fossils, including hominin remains of *Homo* sp. *aff. heidelbergesis* and *Homo antecessor* (ca. 800-900 ka), and lithic tool assemblages in a stratigraphic context that spans almost one and a half million years (e.g. Carbonell et al., 1999; Berger et al., 2008; Bermúdez de Castro et al. 2010; Rodríguez et al. 2011; Ollé et al., 2013). The multilevel karst system of Atapuerca hosts a practically continuous paleontological succession from the Early and Middle Pleistocene, with stratigraphic sequences thicker than 15 - 20 cm that record environmental, chronological, faunal, human and cultural evolution. The multidisciplinary approach of the Atapuerca Team on Quaternary Research has shown that the high-resolution records give evidence of the continuity and configuration of the human populations throughout Southwestern Europe (e.g. Carbonell et al., 2010; Cuenca-Bescós et al., 2011; Bermúdez de Castro and Martinón-Torres, 2013; Mosquera et al., 2013).

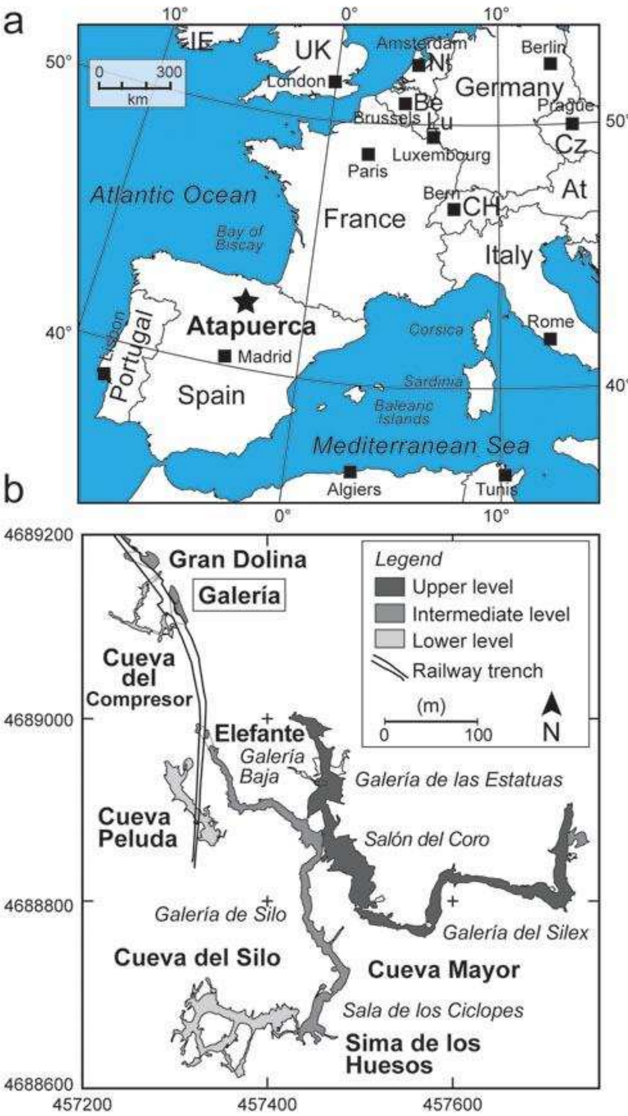

Figure 1. (a) Location of the Sierra de Atapuerca karst system in Northern Spain and (b) the main prehistoric sites in the Atapuerca paleo-archeological site. Gran Dolina, Galería, Cueva

del Compresor, Elefante and Cueva Peluda are located along the Trinchera del Ferrocarril. UTM coordinates are used in (b) (modified from Ortega et al. (2013)). Abbreviations: At – Austria; Be – Belgium; CH – Switzerland; Cz – Czech Republic; IE – Ireland; Lu – Luxemburg; Nl – Netherlands, and UK – United Kingdom.

Ferromagnetic minerals (*sensu lato*) in sedimentary sequences reflect environmental formation conditions. The type and concentration of magnetic minerals are related to environmental factors, such as erosion, wind activity, rainfall or hydrodynamic forces, biological productivity, as well as post-depositional processes, such as dissolution, diagenesis, iron mobilisation or precipitation (e.g. Maher and Thompson, 1999; Evans and Heller, 2003; Liu et al., 2012a).

Cave deposits have been studied using various magnetic methods: magnetic studies of clastic sediments deposited in caves for paleoclimatic and paleoenvironmental reconstructions (e.g. Ellwood et al., 2001; Sroubek et al., 2007; Djerrab and Aïfa, 2010; Warrier et al., 2011; Pennos et al., 2014; Temovski et al., 2016), mineral magnetic studies of burned cave sediments (e.g. Kean et al., 1997; Carrancho et al., 2012; Herrejón et al., 2019) and dating clastic cave sediments using magnetostratigraphic correlation (e.g. Pospelova et al., 2007; Hajna et al., 2010; Pruner et al., 2010; Herries and Shaw, 2011; Bosák et al., 2011; Häuselmann et al., 2015; Bella et al., 2019). At the Atapuerca archeological site, Carracedo et al. (1987), Parés and Pérez-González (1999) and Parés et al. (2000, 2006) reported crucial magnetostratigraphic results for the Gran Dolina, Sima de los Huesos, and Sima del Elefante caves (cf. Fig. 1) and established the occurrence of the Matuyama/Brunhes polarity reversal. A magnetic fabric study of Galería, Gran Dolina and Sala de los Cíclopes (Parés et al., 2010) revealed a higher degree of anisotropy in autochthonous deposits compared to allochthonous deposits and suggested a stronger hydrodynamic regime in the former.

Our research is focused on the sedimentary succession of the Galería Complex, Atapuerca site, Spain. Most of the archeological units of the Galería site date back to the late Middle Pleistocene (Grün and Aguirre, 1987; Falguères, 1986; Falguères et al., 2001, 2013; Berger et al., 2008; Demuro et al., 2014). This study aims to obtain a high-resolution paleoclimatic and paleoenvironmental record in the Galería Complex and to correlate the stratigraphic units with the stages and substages of global climatostratigraphy. Paleoenvironmental conditions during the late Middle Pleistocene glacial and interglacial phases (especially between MIS10 and early MIS7) on the northern Iberian Peninsula are reconstructed in detail.

2. Regional setting

2.1 (Paleo)climatic characteristics

The Sierra de Atapuerca (Atapuerca Range) is located to the north of the Meseta plain at an altitude of 1085 meters above sea level (masl), in the province of Burgos (N Spain). Today, this area is part of a climatic zone C_{fb} following the Köppen-Geiger classification modified by Peel et al. (2007), which corresponds to a temperate climate with dry seasons and temperate summer. The mean annual temperature and precipitation calculated for Atapuerca during the period 1981-2010 were 9.9 ºC and 646 mm/year, respectively (Agencia Española de Meteorología, AEMET).

The Iberian Peninsula has a variable climate resulting from several factors: 1) the geographic location between two large continental masses and between the Atlantic Ocean and the Mediterranean Sea at the southern border of the temperate zone; 2) the influence of Mediterranean, Atlantic and subtropical air masses; 3) the general Northern Hemisphere atmospheric circulation pattern, e.g. the Mediterranean and the North Atlantic Oscillation, which have high interannual climatic variability; and 4) the orography (e.g. Moreno, 2005;

Vicente-Serrano et al., 2017). The Iberian Peninsula possesses a relatively wide coastal area and a central plain with a mean altitude of 650 masl that is segmented by several mountain ranges with altitudes up to 2000 m. Hence, the climate regimes vary across the Iberian Peninsula. Subtropical climate influences increase and temperate conditions decrease from north to south, and Mediterranean air masses predominate Atlantic air masses increasingly from West to East. The interior of the peninsula (Spanish Meseta) has a typical continental climate.

Glacial-interglacial climate variations are expected during the Pleistocene for the Iberian Peninsula (Blain et al., 2018). Numerous caves developed in the Sierra de Atapuerca in the Middle Pleistocene (Demuro et al., 2014) when warmer than present day mean temperatures prevailed. These caves are generally thought of as important centres of biotic refugia (Hewitt, 1999; Blain et al., 2018).

Consistent with most terrestrial records presented by the Past Interglacials Working Group of PAGES (2016), Blain et al. (2018) reconstructed mean annual temperature (MAT) and mean annual precipitation (MAP) for Atapuerca and proposed a less warm MIS9 compared to the warm MIS11c, although MIS9 was still significantly warmer (ΔMAT +2.8 °C) than the present MAT in Burgos city near the Atapuerca excavation sites. The MAP in MIS9 also was higher than present (ΔMAP + 292 mm). The (temperate) Mediterranean landscape may have been characterized by a mosaic of dry meadows, rocky or stony areas, open scrubland and quiet rivers with gallery forests (20%). Possible unrecognized hiatuses of the cave sediment sequences (e.g. in the smooth transition between MIS9 and MIS8) may have caused difficulties for correlating the various sites and units of the Iberian Peninsula with global marine records (Blain et al., 2018).

2.2 Geological setting

In the “Sierra de Atapuerca”, a cave system has developed in Upper Cretaceous limestones and dolomites (Fig. 1b). Geomorphologic and speleogenetic studies (Benito-Calvo et al., 2008, 2017; Ortega, 2009; Ortega et al., 2013, 2014) indicate that this cave system contains three inactive subhorizontal passages interconnected by shafts and chambers (Fig. 1b). These multilevel caves are perched at around +90 m, +70 m, and +60 m above the current course of the Arlanzón River and were cut in association with Plio-Pleistocene fluvial base levels (Ortega et al., 2013).

At present, 4.7 km of passages in the Cueva Mayor-Cueva del Silo system, Cueva Peluda, and Cueva del Compresor caves, as well as many sediment covered cave entrances, have been explored in the Atapuerca cave system (Ortega et al., 2013) (Fig. 1b). Some of these caves, including Gran Dolina, Galería, and Sima del Elefante, were discovered in an early 20th century railway trench. The Galería Complex (42º 21’ 5’’ N lat., 3º 31’ 11’’ W long.), which is situated about 50 m south of Gran Dolina, corresponds to the vestibule of an old cave that is exposed on the eastern railway trench wall and its occupation is associated with the middle karst level (Fig. 1b) (Ortega et al., 2014). It has been partially excavated from 1979 to 1995 and from 2002 to present. Typical cave infill sediments with faunal remains and lithic artefacts were discovered in a well-established stratigraphic context (Pérez-González et al., 1999; Carbonell et al., 1999; García-Medrano et al., 2017). The cave now opens to the top (Fig. 2).

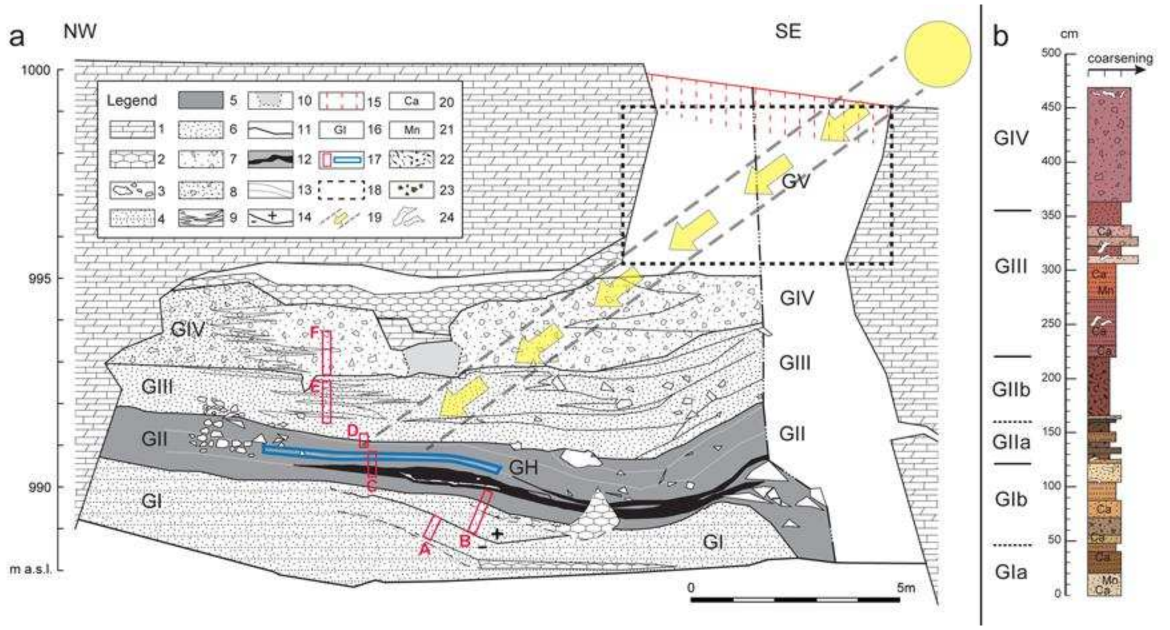

Figure 2. Studied section. (a) Cross-section of the Galería cave and its deposits (modified after Ortega (2009)). (b) Detailed stratigraphic subdivision of the studied sequence. Legend: (1) Upper Cretaceous limestone and dolomite (wall of Galería cave); (2) speleothems; (3) limestone blocks and cobbles; (4) fine-grained material of unit GI; (5) dominantly clayey/silty material of unit GII; (6) fine sediment of unit GIII; (7) sediment with gravel/breccia (unit GIV); (8) lateral facies variation dominated by clay loam (poorly sorted clayey-sandy silt in equal proportion); (9) lateral facies variations from clay loam to gravel (left-hand side) and from gravels to breccia (right-hand side); (10) cut and fill; (11) major stratigraphical boundaries; (12) bat guano level; (13) limit of unit GII layers; (14) Matuyama-Brunhes reversal boundary (Pérez-González et al., 2001); (15) recent soil; (16) main stratigraphic units; (17) red sampling profiles A - F represent the study section and cross stratigraphic layers GI - GIV, whereas the blue horizontal profile GH was sampled to investigate the possible influence of solar irradiation on sediment magnetism; (18) cross-section of the model sinkhole for (19) solar irradiation calculations (see Supplement 2 and text below); (20) secondary carbonate; (21) manganese patches and concretions; (22) strong clayey (pedogenic) structure; (23) clayey (pedogenic) fragments; and (24) speleothem debris. The yellow circle symbolizes the Sun, i.e. solar irradiation source. A colour figure can be found in the online version, and detailed information about the stratigraphic units (e.g. Munsell colour) is provided in Supplement 1.

The sedimentary infill of the Galería consists of five lithostratigraphic units (from bottom to top) called GI to GV and a soil developed on unit GV (Fig. 2a and b). Unit GI (closed cave unit; subunits GIa and GIb) represents mainly an interior or autochthonous facies of laminated silts, limestone breccia and speleothems related to flowing or stagnant waters. The top of GI is composed of massive and bioturbated interbedded clastic sandy facies, with mud-balls from the reddish-brown lower clay substrate (Pérez-González et al., 1995), which may have been deposited in a high-energy hydrodynamic regime and under some external influence. In addition, an interstratified thin and discontinuous layer of bat guano occurs at the top. This unit does not contain fauna and is archeologically sterile.

GII, GIII and GIV (open cave units) are allochthonous units that fill the section of the cavity (Fig. 2) and were generated by gravity flows and erosional processes (e.g. sheet-wash) under an external influence. They are separated from each other by erosional unconformities and consist of heteromorphic carbonate clasts and debris flows that transform northward into detrital facies of fine laminated sandy clay-loam. The latter facies interfinger with debris flow facies derived from further north. Organic facies formed of bat guano interstratified with red shales are found at the bottom of GII (subunit GIIa) (Fig. 2b). In addition, fallen limestone blocks give evidence of the event that opened the cave ceiling. Polygonal patterns are observed in the red clay GIIb horizon. Such polygonal patterns may be related to exsiccation (e.g. seasonal drying) or permafrost activity. No sign of cryoturbation or any other marks of intense permafrost have been observed in the unit, which supports the interpretation of exsiccation by seasonal drying. Units GII and GIII both contain hominin tools and fauna. The top of the cavity infill (units GIV and GV) also consists of heterogeneously sized limestone clasts (Pérez-González et al., 1999, 2001; Valverdú, 1999; Valverdú i Poch, 2017). A more detailed description of the Galería Complex stratigraphy can be found in Vallverdú i Poch (2017) and references therein.

Parés et al. (2010) correlated their magnetic susceptibility anisotropy results with higher hydrodynamic forces during the deposition of unit GI and quiet depositional conditions in unit GIII. The GI–GII boundary is coeval with the collapse that generated an opening in the ceiling of the Galería cave. This opening, which is about 6 m wide and is probably due to a transverse fracture, allowed material input from cave surroundings (Fig. 2a). Moreover, it acted as a window that allowed solar irradiation into the cave.

The Matuyama-Brunhes polarity transition (770.2 ± 7.3 ka; Suganuma et al., 2015; Singer et al., 2019) was detected in unit GI (Pérez-González et al., 2001), whereas units GII to GIV have been dated by thermoluminescence and infrared stimulated luminescence (IRSL) from 503 ± 95 ka at the bottom of GII to 185 ± 26 ka at the top of GIV (Berger et al., 2008). The speleothem overlying unit GIV in the central Galería Complex has been dated by uranium series at 118 +71/-49 ka and by electron spin resonance (ESR) at around 200 ka, and ages earlier than 350 ka have been assigned by the same methods to the GII base and GI top (Falguères, 1986; Falguères et al., 2013; Grün and Aguirre, 1987) (Fig. 2). The existing chronological data, based on both ESR and optically stimulated luminescence (OSL) methods, suggest uninterrupted sedimentation from units GIb to the base of GIV (Demuro et al., 2014). A sedimentary hiatus divides unit GI into two subunits, since the Matuyama-Brunhes boundary was observed between subunits GIa and GIb, and ages in GIb are much younger (350 – 400 ka). The archeological interest of the site lies in the hominid fossils found in units GII and GIII (Carbonell et al., 1999), which have a paleontological Middle Pleistocene age, in bones of *Homo heidelbergensis* (Arsuaga et al., 1999; Rosas and Bermúdez de Castro, 1999) (Fig. 2), in Mode 2 industries (Acheulean) (Ollé et al., 2013; García-Medrano et al., 2017) and in GIII soils that contain evidence of archeological occupation (Lorenzo and Carbonell, 1999).

3. Material and methods

3.1. Sampling

Non-oriented and unconsolidated samples were taken at 4 – 8 cm intervals across a 500 cm composite profile in the north-central cavity, near the cave's ceiling entrance (Fig. 2). Each sample represents a 3 – 4 cm thickness of various horizons (Supplement 1). The magnetic properties of 87 samples were measured. In the laboratory, grain-sizes smaller than 1 mm were separated by sieving. The remaining samples were packed into 3.6 cm^3 cylindrical plastic boxes and were weighed for rock magnetic analysis. Magnetic measurements were carried out at the Paleomagnetic Laboratory of Burgos University (Spain) and at the Laboratory for Natural Magnetism, ETH Zürich (Switzerland).

3.2. Room temperature experiments

Mass specific magnetic susceptibility (χ) was measured using a Kappabridge KLY-2 system (AGICO). A dual frequency (0.47 and 4.7 kHz) MS2 susceptibility meter (Bartington Instruments) was used to determine the relative frequency dependent susceptibility (χ_{fd}%; Maher, 1986; Dearing et al., 1996a):

$$\chi_{fd}\% = 100\frac{\chi_{fd}}{\chi_{lf}}, \quad (1)$$

where $\chi_{fd} = \chi_{lf} - \chi_{hf}$ and χ_{lf} and χ_{hf} are the low field magnetic susceptibility measured at low and high frequency, respectively. This parameter indicates the contribution of fine-grained magnetite (near the SP/SD boundary, where SP = superparamagnetic and SD = stable single domain states) (Dearing et al., 1996a). Anhysteretic remanent magnetization (ARM) was induced in a peak alternating field (AF) of 140 mT in the presence of a direct current (DC) bias field of 0.1 mT using an AF demagnetization device coupled to a 2G Enterprises cryogenic magnetometer. The susceptibility of ARM (χ_{ARM}) was obtained by dividing the

ARM by the DC bias field. Next, samples were subjected to stepwise isothermal remanent magnetization (IRM) acquisition up to 2 T (IRM_{2T} or SIRM) using a pulse magnetizer.

Frequency dependent susceptibility (χ_{fd}%) and χ_{ARM}/SIRM have been used to analyze the grain size distribution of ferrimagnetic components (magnetite and/or maghemite) (e.g. Maher and Taylor, 1988; Maher and Thompson, 1999; Evans and Heller, 2003). To avoid the high coercivity mineral contribution and to assure that the same magnetic components affect both χ_{ARM} and IRM, we use the IRM acquired at 100 mT ($IRM_{0.1T}$) instead of SIRM (Geiss et al., 2008).

Eleven selected samples that were subjected to ARM experiments were demagnetized by applying progressive AF demagnetization up to 140 mT. Next, they were subjected to stepwise IRM acquisition up to 2 T with a pulse magnetiser and subsequently stepwise AF demagnetized up to 300 mT and measured on a 2G Enterprises cryogenic magnetometer model 755. Unmixing coercivity distributions resulting from ARM and IRM demagnetization curves (Robertson and France, 1994; Egli, 2003) were performed using the MAX UnMix software (Maxbauer et al., 2016a), with SGG (skewed generalized Gaussian) functions (Egli, 2003, 2004). Each coercivity component is characterized by the median destructive field ($B_{1/2}$ or MDF) or peak of the coercivity distribution, the dispersion parameter (DP), the relative extrapolated contribution of each component to the total magnetization (EC), and a parameter describing skewness (S) (Egli, 2004; Maxbauer et al., 2016a).

A variable field translation balance was used to measure IRM acquisition and back-field coercivity curves, hysteresis loops (± 1T), and thermomagnetic curves. The latter were measured by heating in air to 700 °C in a 38 mT constant field and were then cooled to room temperature. Hysteresis parameters were calculated using the RockMagAnalyzer 1.0 software (Leonhardt, 2006). Finally, representative samples were consolidated using plaster and were subjected to thermal demagnetization of a composite three-axis IRM (orthogonally induced at

2, 0.4, and 0.12 T, respectively) according to the method proposed by Lowrie (1990) following Márton et al. (1980).

3.3. Low temperature experiments

Techniques that employ remanence measurements at room and low temperatures to avoid chemical alteration have been used in environmental magnetism to infer magnetic mineralogy and granulometry (e.g. Banerjee et al., 1993; Fang et al., 1999; Dearing et al., 1997; France and Oldfield, 2000; Maher et al., 2004; Lagroix and Guyodo, 2017). In this study, we use the method of Bógalo et al. (2001) to calculate the following proxies (see Supplement 2). Grains near the SP/stable SD boundary at room temperature can became blocked thermally when cooled to 77 K, so the following parameter is defined:

$$SP_{LC} = (IRM_{LL} - IRM_{RL})_{0.1T} \,, \qquad (2)$$

where SP_{LC} ("LC" = low coercivity) indicates the total magnetization of ferrimagnetic minerals in the SP state. These fine low coercivity minerals can be related to pedogenic (or also bacterial) magnetite/maghemite. IRM_{LL} denotes IRM values induced in a relatively small field (0.1 T) and measured both at low temperature (77 K; ca. -196 °C; "L" subscript) and IRM_{RL} when the remanence was acquired in a 0.1 T field at room temperature (293 K; ca. 20 °C; "R" subscript) and measured at low temperature (77 K) (Bógalo, 1999; Bógalo et al., 2001; and Supplement 2). The relative content of SP grains in the ferrimagnetic fraction can be expressed by the normalized ratio:

$$SP\%_{LC} = 100 \cdot \frac{(IRM_{LL} - IRM_{RL})_{0.1T}}{(IRM_{LL})_{0.1T}} \,. \qquad (3)$$

To estimate the contribution of ferrimagnetic SP grains, two methods have been used: the frequency dependent magnetic susceptibility (χ_{fd} and $\chi_{fd}\%$) and the difference between remanences acquired at 0.1 T at low and room temperature (SP_{LC} and $SP\%_{LC}$) (Fig. 6 and Fig. S3 in Supplement 2). The relative frequency dependent susceptibility ($\chi_{fd}\%$) is diagnostic of the presence of SP ferrimagnetic grains near the SP/SD threshold size, which is related to pedogenic mineral formation (e.g. Forster et al., 1994; Dearing et al., 1996a; Liu et al., 2004; Long et al., 2015). However, if the magnetite content is low, paramagnetic and MD (multidomain) ferrimagnetic mineral fractions, whose susceptibility is frequency independent, may lower χ_{fd} values considerably (Hrouda, 2011). Determination of SP_{LC} and $SP\%_{LC}$ enables us to check the interpretation of frequency dependent susceptibility because paramagnetic grains do not contribute to remanence and when the possible presence of MD grains can be evaluated (Bógalo et al., 2001 and Supplement 2).

A comparison of IRM acquired at room temperature in a 2 T field (well above the saturation field of ferrimagnetic minerals) and measured at room temperature (IRM_{RR}) with the same IRM measured at low temperature (IRM_{RL}) is denoted as the G parameter (see Supplement 2). This comparison is based on the fact that goethite is the only magnetic mineral whose spontaneous magnetization strongly increases with decreasing temperature below 20 °C. Therefore:

$$G = (IRM_{RL} - IRM_{RR})_{2T} \,. \tag{4}$$

This parameter can be taken as a proxy for evaluating the presence of goethite. A normalized version of this parameter enables evaluation of the relative goethite content:

$$g\% = 100 \cdot \frac{(IRM_{RL} - IRM_{RR})_{2T}}{(IRM_{RL})_{2T}} \,. \tag{5}$$

A possible contribution of antiferromagnetic SP minerals (goethite and/or hematite) can be deduced by comparing the increase in the slope of IRM_{LL} acquisition and IRM_{RL} curves, following Bógalo et al. (2001) (see Supplement 2):

$$SP_{HC} = (IRM_{2T} - IRM_{0.1T})_{LL} - (IRM_{2T} - IRM_{0.1T})_{RL} \,. \tag{6}$$

The term in the second set of parentheses is the remanence increase in goethite due to any increase of spontaneous magnetization with decreasing temperature. The term in the first set of parentheses is controlled by both the variation in goethite spontaneous magnetization and

SP behaviour in antiferromagnetic grains at 293 K that becomes blocked when cooled to 77 K.

The percentage of antiferromagnetic SP contribution will be:

$$SP\%_{HC} = 100 \cdot \frac{(IRM_{2T} - IRM_{0.1T})_{LL} - (IRM_{2T} - IRM_{0.1T})_{RL}}{(IRM_{2T} - IRM_{0.1T})_{LL}} . \qquad (7)$$

Therefore, low (magnetite/maghemite) and high coercivity (goethite/hematite) minerals in different magnetic states can be estimated quantitatively using low temperature IRM experiments.

4. Results

4.1 Rock magnetic results

The low field, bulk magnetic susceptibility χ_{lf} includes contributions from dia-, para-, ferri- and antiferromagnetic minerals. To verify the significance of the ferrimagnetic contribution, the relationship χ_{lf} vs. $(IRM_{2T})_{RR}$ (ferrimagnetic proxy; see Methods and Fig. S1, Supplement 2) was used. It has a strong linear correlation between χ_{lf} and the ferrimagnetic components (correlation coefficient $r^2 > 0.95$).

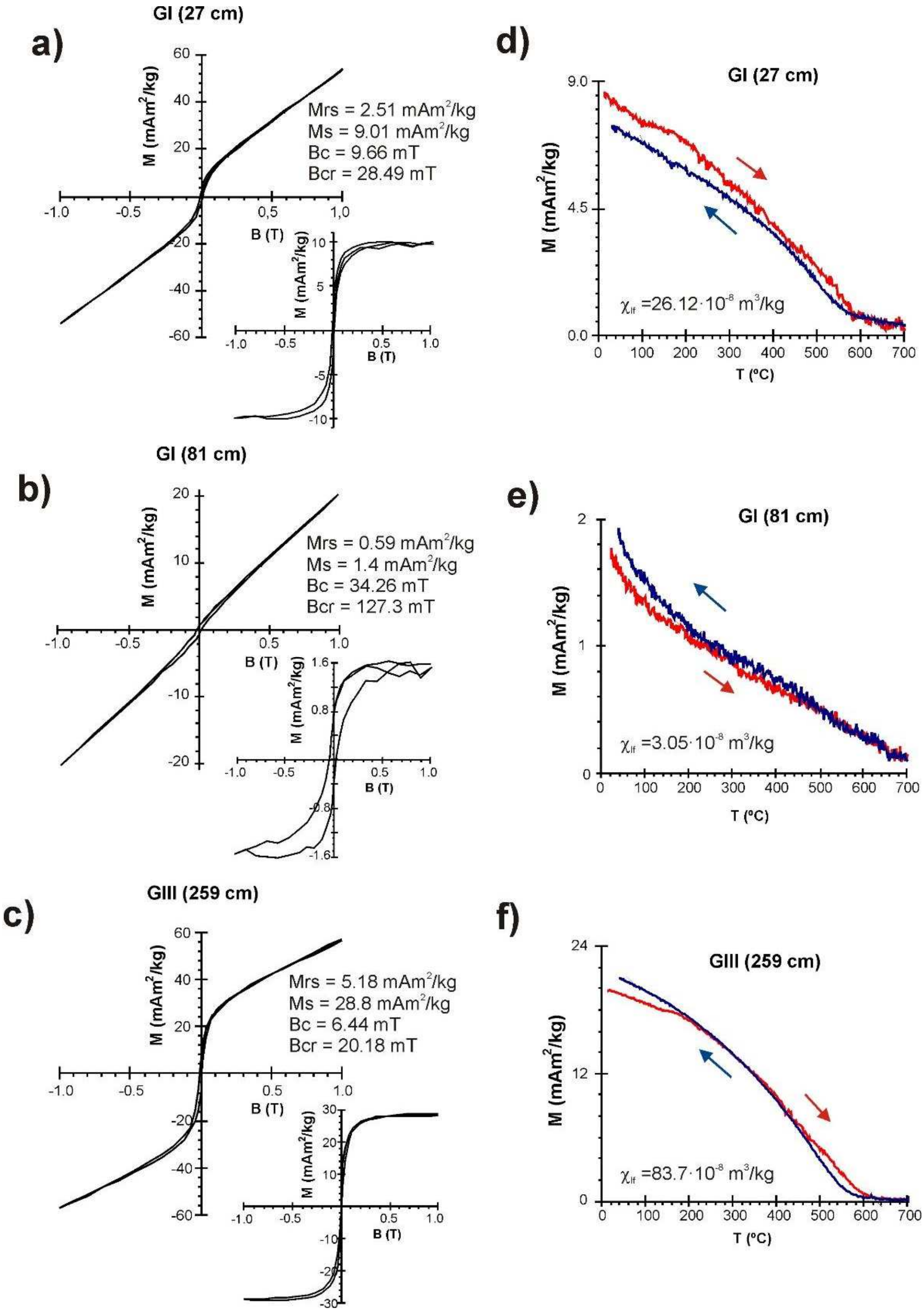

Figure 3. Rock magnetic characteristics (I). Hysteresis loops (a, b, and c with insets of loops corrected for high-field contributions and strong-field thermomagnetic curves (d, e, and f) for three selected samples from the Galería profile. Note the high coercivity contributions, especially in samples from unit GI (interior facies). The nearly reversible thermomagnetic curve for unit GIII with well-defined Curie temperature around 580 °C is also common in units GII – IV (entrance facies).

Wasp-waisted hysteresis loops are observed for most of the measured samples (Figs. 3a, b, and c). They are usually interpreted as a mixture of magnetic minerals with different coercivities or in different domain states (Roberts et al., 1995). Hysteresis loops for samples from unit GI and a few from lower part of unit GII do not close at fields above 0.5 T (Figs. 3a and b). Hysteresis loops for the remaining samples from units GII to GIV close at 0.2 – 0.3 T (Fig. 3c).

The most common feature of the heating curves identified in most samples is a gradual magnetization decrease from room temperature that reaches near-zero values at 560 – 580 °C, which is the Curie temperature (T_c) of magnetite (Figs. 3d and f). Some samples have a magnetization left above 580 ºC that fades at around 660 – 680 ºC, which is characteristic of hematite. A hyperbolic heating curve is observed in some weakly magnetic samples between room temperature and 350 ºC (Fig. 3e), which confirms the substantial paramagnetic contributions to the high-field slope of hysteresis curves (e.g. Fig. 3b). In some curves, a small inflection is identified between 160 and 250 ºC, and the maximum is at around 180 – 200 ºC (Figs. 3d and f). Thermomagnetic curves for all samples, except for two from the upper part of unit GI and the lower part of GII, are mostly reversible.

Thermal demagnetization of a 3-axis IRM with 17 temperature steps between room temperature and 680 °C was performed (Figs. 4a, b, and c). The soft component (0.12 T applied field) has a maximum unblocking temperature between 580 and 600 ºC. The intermediate coercivity component (0.4 T) for most samples unblocks at around 300 ºC. The highest coercivity component (2 T) has maximum unblocking temperatures of 80 – 120 ºC and > 650 ºC. Despite these similarities, samples from the lowest part of unit GI and from units GII to GIV (with exceptions at 143 and 341 cm), have an initially soft magnetization component (0.12 T) up to 10 times stronger than those of the intermediate and hard components (Figs. 4a and c). On the other hand, samples from the upper part of unit GI (GIb, 81 cm), which have low susceptibility, have similar initial remanence intensities along the three axes (Fig. 4b).

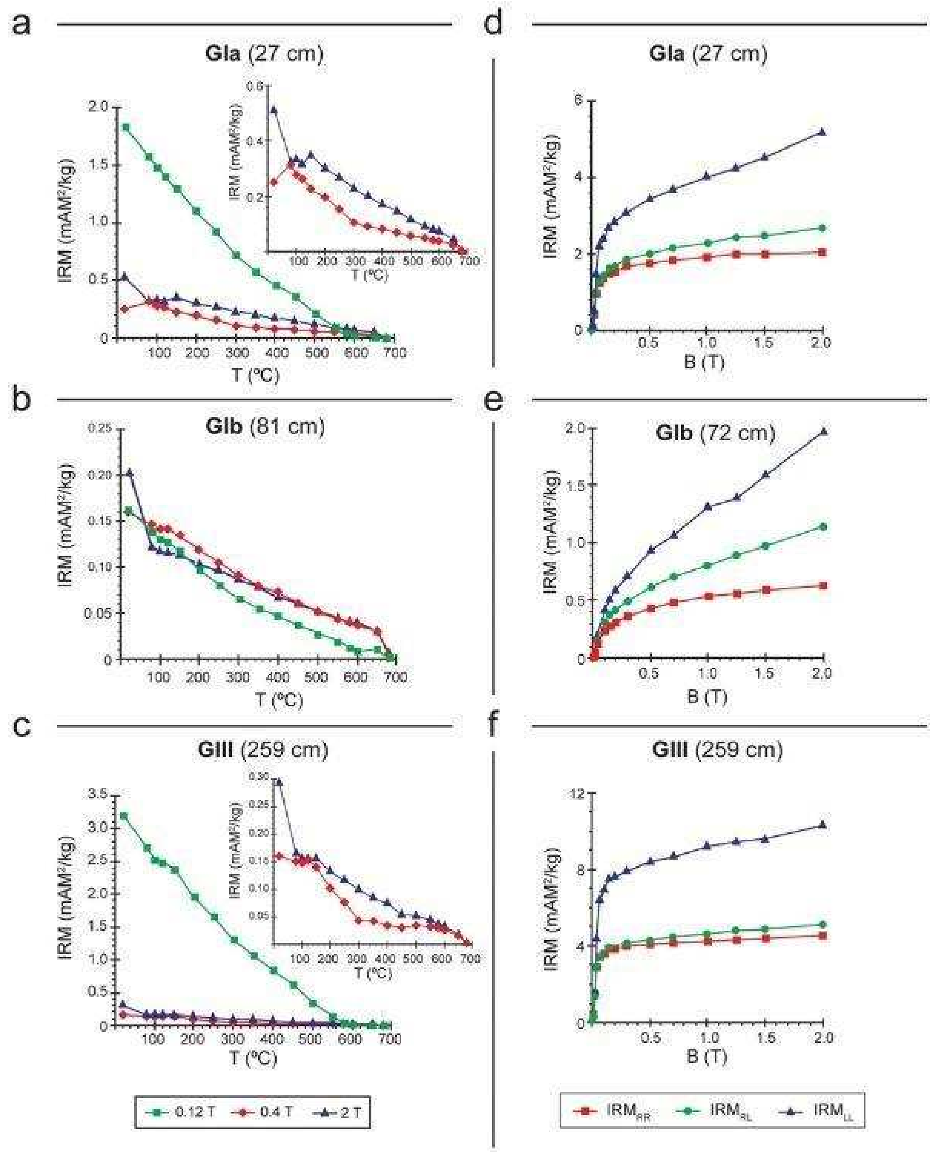

Figure 4. Rock magnetic characteristics (II). a–c) Thermal demagnetization of a 3-axis IRM (IRM_{RR}) imparted in fields of 2.0, 0.4, and 0.12 T. The three samples have contributions from magnetite in the soft component and goethite and hematite in the hard component. Intermediate and hard components are expanded for clarity in insets for samples with high magnetite concentrations (a and c). d–f) IRM acquisition at room (20 °C) and liquid nitrogen temperatures (-196 °C). Note that the first IRM subscript denotes the temperature (L = low or R = room) at which remanence was acquired and the second denotes the temperature at which remanence was measured: IRM_{RR}: remanence acquired and measured at room temperature

(20 °C); IRM_{RL}: remanence acquired at room temperature and measured at low temperature (-196 °C) and IRM_{LL}: remanence acquired and measured at low temperature.

IRM acquisition curves measured at 293 K and 77 K (Figs. 4d–f) indicate two characteristic behaviour types (see Supplement 2). 1) IRM_{RR} curves (red squares) for samples from the bottom of GI and units GII to GIV are nearly saturated at around 100 mT (Figs. 4d and f). When the remanence is measured at low temperature (green dots: IRM_{RL}), a small increase of the slope of the curve with respect to IRM_{RR} is observed but the difference IRM_{RL} – IRM_{RR} at 100 mT is small or negligible. At low temperatures, IRM_{LL} (blue triangles) has much higher intensity than IRM_{RR} at low fields (100-200 mT) and an additional increase of slope with respect to the IRM_{RL} curve. 2) IRM_{RR} curves for several samples from unit GI, especially for low susceptibility samples (Fig. 6a) that do not saturate at the maximum field of 2 T (Fig. 4e). Both the remanence intensity and slope of the IRM curve increase strongly at low temperatures, and IRM_{LL} imprinted and measured at 77 K is much more enhanced.

Unmixing of AF demagnetization curves of IRM and ARM provides information about the coercivity distributions of magnetic components. The decomposed curves and the characteristic parameters are shown in Supplement 2 (Fig. S2 and Table S1). The first derivative of the ARM demagnetization curve can be fitted by a single component (Comp. 1) in nine of the eleven analysed specimens. This component has a median destructive field of ARM (MDF_{ARM}) between 20.6 mT (dispersion parameter DP = 0.28) and 15.6 mT (DP = 0.28). Samples from unit GI (49 and 72 cm) have been fitted with two components. The low coercivity component has similar MDF_{ARM} values as other specimens and accounts for 86% of the ARM, although an additional higher coercivity component (Comp. 2) is necessary to obtain a good fit. This component has MDF_{ARM} values of 107.3 mT (DP = 0.28) and 94.6 mT (DP = 0.21). All IRM demagnetization curves can be decomposed using a two-component model. Comp. 1 has MDF_{IRM} between 16.3 mT (DP = 0.29) and 27 mT (DP = 0.36). Comp. 2

has different mean coercivities depending on the unit. Samples from unit GI (49 and 72 cm) were fitted with a component with MDF_{IRM} of 624.2 mT (DP = 0.47) and account for up to 65% of the IRM, whereas samples from the other units have values between 286.5 mT (DP = 0.58) and 75.6 mT (DP = 0.79).

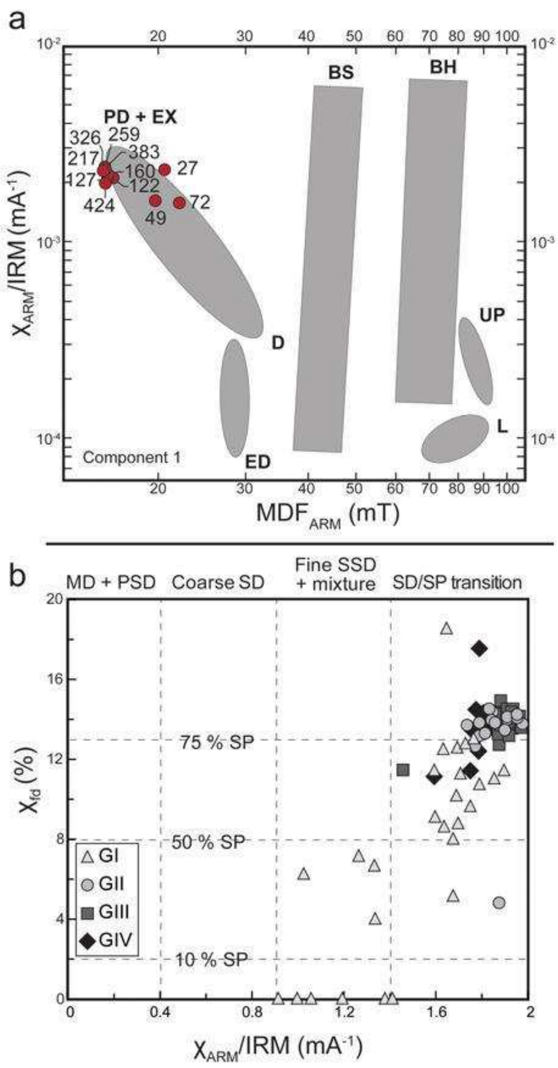

Figure 5. Rock magnetic characteristics (III). a) Unmixing results of MDF_{ARM} projected onto an Egli diagram (Egli, 2004). Numbers close to the symbols indicate sample height (cf. Fig. 2). PD+EX = pedogenic + extracellular magnetite, D = detrital particles, BS = biogenic soft, BH = biogenic hard, ED = eolian dust, L = loess, and UP = atmospheric particulate matter produced by urban pollution. b) Semiquantitative plot of χ_{fd} (%) versus $\chi_{ARM}/IRM_{0.1T}$ (Dearing et al., 1997).

Results for the low coercivity component (Comp. 1) from the decomposed ARM and IRM curves are compiled in Table S1 and plotted partly in the Egli diagram (Fig. 5a), which assigns different field regions to different magnetic mineral types in sediments (Egli, 2004). χ_{ARM}/IRM for component 1 plotted against MDF_{ARM} in Fig. 5a. Higher χ_{ARM}/IRM values indicate finer magnetic grain sizes up to fine SD particles (e.g. Maher, 1988; Peters and Dekkers, 2003). All samples, except those from unit GI, are well grouped into the area for PD+EX particles (Egli, 2004). This result is also supported by Fig. 5b where χ_{fd}% (an indicator of the relative amount of ferrimagnetic SP grains is plotted versus $\chi_{ARM}/IRM_{0.1T}$ (Dearing et al., 1997). Samples from units GII to GIV are well grouped in the right-hand corner of the plot with χ_{fd}% values between 12 and 15 % and χ_{ARM}/IRM values higher than 1.6×10^{-3} m/A. Results from unit GI are more scattered with lower χ_{fd}% values.

4.2 Stratigraphic distribution of magnetic parameters

Stratigraphic profiles of magnetic properties are shown in Fig. 6 and Fig. S3. In unit GI, parameters related to the bulk magnetic mineral concentration, such as χ (Fig. 6a, b), χ_{ARM} and $(IRM_{2T})_{RR}$ (Fig. S3), have higher values in the lowermost part, whereas χ values are one-fiftieth of those in the overlying units GII to GIV. The variable magnetic mineral concentration in lower unit GII (GIIa) reaches maximum values at the bottom of unit GIIb. From the middle of unit GII to unit GIV, these parameters decrease gradually upward and are more homogeneous. The room temperature ratio $IRM_{0.1T}/IRM_{2T}$ (Fig. 6c) in unit GI differs from that in units GII to GIV.

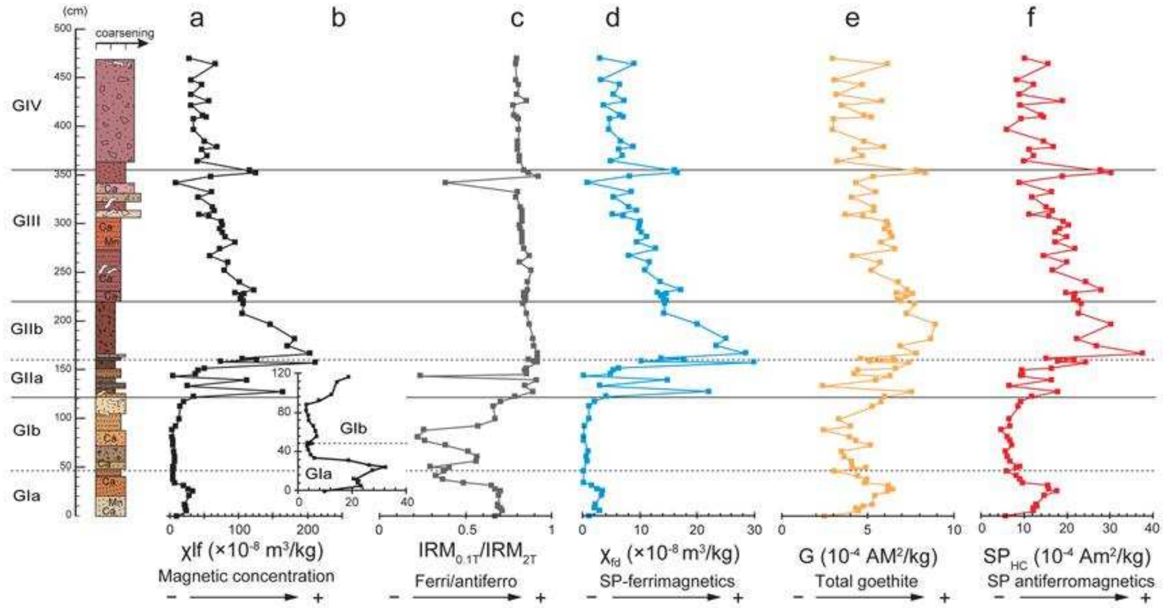

Figure 6. Stratigraphic distribution of selected magnetic parameters along the composite profile from Galería cave. a) Low-field magnetic susceptibility χ_{lf}; b) enlarged low-field magnetic susceptibility χ_{lf} for units GIa and GIb; c) $IRM_{0.1T}$ /IRM_{2T}, both measured and acquired at room temperature (293 K); d) frequency dependent susceptibility χ_{fd}; e) total goethite content G; and f) total antiferromagnetic SP content. Lithological units to the left are as in Fig. 2.

The absolute SP content in the ferrimagnetic mineral fraction estimated by χ_{fd} (Fig. 6d) and SP_{LC} (Fig. S3) follows a similar pattern as χ or $(IRM_{2T})_{RR}$ (Fig. 6a and Fig. S3). The low χ_{fd} and SP_{LC} values in unit GI increase rapidly from the bottom of unit GII to 150–170 cm and then decrease toward the youngest unit. χ_{fd}% (Fig. S3) varies between 19 and 4% in unit GI, although it is nearly uniform from unit GII to GIV, with values around 14% (exceptions at 158 and 431 cm). All goethite parameters G and g% (eq. #4 and 5) are positive and range mostly between 2.5 and 6 × 10^{-4} Am^2/kg, except for the upper part of unit GII (Fig. 6e). Hence, although the presence of hematite might smooth the increased IRM_{RL} values, goethite is omnipresent. The relative goethite concentration (g%) (Fig. S3) has high values in unit GI, which has the lowest χ, χ_{ARM} and $(IRM_{2T})_{RR}$ values (Fig. 6) because of its low ferrimagnetic mineral concentration. The g% profile mirrors $IRM_{0.1T}$/IRM_{2T}. The absolute contribution of antiferromagnetic SP grains (SP_{HC}) (Fig. 6f) has a maximum in unit GII at the same position as the peak of ferrimagnetic SP grains (χ_{fd} in Fig. 6d) and SP_{LC} (Fig. S3). The percentage of antiferromagnetic SP grains ($SP\%_{HC}$ in Fig. S3) is homogeneous from unit GII to GIV, with only one exception at 347 cm (topmost unit GIII).

5. Discussion

5.1 Magnetic mineral identification

The significant linear correlation of $(IRM_{2T})_{RR}$ and χ (Fig. S1, Supplement 2; correlation coefficient $r^2 > 0.95$) indicates that the magnetic parameters are controlled predominantly by ferrimagnetic minerals, which is characteristic of soils that developed in warm and moist temperate continental and Mediterranean climates (Jordanova, 2016). However, the general similarity between $\chi_{fd}\%$ and $SP\%_{LC}$ (Fig. S3) indicates that paramagnetic, diamagnetic, and MD ferromagnetic *s.l.* contributions play a subordinate role. Magnetite is the main ferrimagnetic contributor as indicated by the pre-dominating magnetic phase with Curie temperature of 560 – 580 ºC (Fig. 3d–e) and maximum unblocking temperatures between 580 and 600 ºC (Fig. 4a–c). The gradual magnetization decrease during heating is typical of a distribution of SD magnetite grains. The occurrence of stable maghemite cannot be excluded because maximum unblocking temperatures of about 600 ºC are also observed (e.g. Özdemir and Banerjee, 1984; Gehring et al., 2009). High values of χ_{fd}, $\chi_{ARM}/IRM_{0.1T}$ and SP_{LC} (Fig. 5b, 6d and S3) indicate a significant fine-grained magnetite concentration (SD/SP) in most samples (e.g. Maher and Taylor, 1988; Forster et al., 1994; Dearing et al., 1996a). High $\chi_{fd}\%$ values are related to pedogenic magnetite (e.g. Dearing, 1996a; Liu et al., 2007). The low coercivity component in the ARM and IRM curves (Comp. 1; Fig. S2) is associated with magnetite-like minerals, for which data always fall into the PD+EX field of the Egli diagram (Fig. 5; Egli, 2004). $\chi_{ARM}/IRM_{0.1T}$ and MDF_{ARM} suggest grain-sizes finer than 0.02 µm (see

Maher, 1988). This component is weak in unit GI and less well grouped (Fig. 5a) because of the presence of fine-grained high coercivity minerals (hematite/goethite).

Fine-grained ferrimagnetic minerals dominate the magnetic signal throughout the profile, although their concentration is low in parts of unit GI, which represent interior cave facies. The open cave sediments of units GII to GIV carry variable SP ferrimagnetic mineral concentrations, with a peak in the bottom of subunit GIIb (depth 150–200 cm). Pedogenic magnetite can be related to allochthonous minerals originating from soil erosion near the cave entrance. Although units GII and GIII contain fossils and evidence of human occupation (Rosas et al. 1998; Carbonell et al. 1999; Ollé et al. 2013), there is no archeological evidence of burned material (Vallverdú, 1999; Huguet et al., 1999). Therefore, we rule out SP magnetite formation as a result of human activity, such as burning.

The profile is near the opening of the cave ceiling, so it is possible that the currently visible large hole was already present during sedimentation and enabled solar irradiation to reach the cave interior (Fig. 2). Solar irradiation controls various environmental factors, such as moisture, temperature or evapotranspiration (e.g. Irmak et al., 2003; Wang and Dickinson, 2012; Helm et al., 2016), and these factors could condition pedogenic processes and the creation/transformation of magnetic grains. In this case, irradiation solid angles subtended by the cave roof opening vary along the horizontal profile GH (blue rectangle in Fig. 2). To test the possible effect of insolation, χ_{fd} as a proxy of pedogenic magnetite was measured along GH. The horizontal profile intersects the vertical profile C at 166 cm height (GIIb) where it is characterized by maximum magnetic proxies such as χ, χ_{fd}, χ_{ARM} and IRM_{2T}. χ_{fd} values along the horizontal transect are plotted against average annual irradiation $H^{(b+d)}$ (beam + diffuse irradiation; see Supplement 2) assuming a circular opening (eccentricity of the opening, e = 0) in Fig. 7. No large boulders or blocks are identified in sedimentary units above the horizontal profile. Therefore, we assume that the hole has not changed significantly during deposition of the GH horizon (5 cm thick) (Fig. 2).

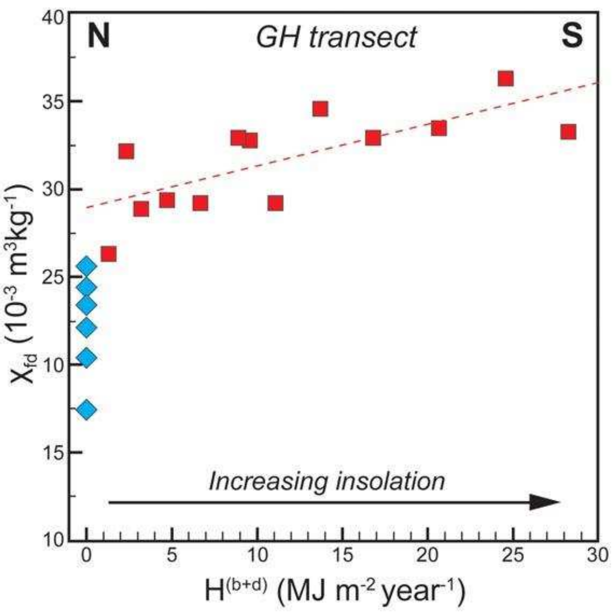

Figure 7. Influence of solar irradiation on magnetic mineral formation: frequency dependent susceptibility (χ_{fd}) vs. annual $H^{(b+d)}$ (beam + diffuse irradiation) plot. The data originate from the horizontal profile GH in Fig. 2 along the level of maximum χ_{fd} in the vertical sequence C (cf. Fig. 6a). Diamonds correspond to sites that receive only reflected radiation. See Supplement 2 for further explanation.

χ_{fd} tends to decrease toward the cave interior (Fig. 7). The positive correlation between irradiation energy and the environmental magnetic proxy allows a possible solar influence on magnetic mineral neoformation in the cave sediments. The reconstructed theoretical solar irradiation into the cave could have favoured intermittent wetting and drying of the sediments to foster the formation of ferrihydrite and subsequent authigenic SP ferrimagnets by a fermentation process in the sediment of units GII and lower part of GIII (e.g. Schwertmann, 1988; Dearing et al., 1996b; Maher, 1998; Barron and Torrent, 2002; Jiang et al., 2018). Some sediment components in units GII to IV stem from surface soil horizons near the cave entrance, which may provide excess iron required for the fermentation process. Thus, pedogenic magnetite/maghemite might have formed in these sediments.

Rock magnetic experiments also document the presence of antiferromagnetic minerals (goethite and/or hematite). The occurrence of hematite is indicated in Fig. 3e and Fig. 4a–c with Curie and maximum unblocking temperatures between 650 and 680 ºC. Unmixed ARM and IRM acquisition curves reveal a high coercivity component (Comp. 2) associated with variable grain-size distributions of goethite+hematite (Supplement 2: Fig. S2). SD goethite has been recognized through several procedures. Thermal experiments reveal a magnetic phase with Curie temperature of around 120 ºC and unblocking temperatures of 80–120 ºC (Fig. 3d and Figs. 4a–c), which are consistent with the occurrence of goethite. The characteristic strong spontaneous magnetization increase of goethite with decreasing temperature is also observed in IRM experiments (Figs. 4d–f). In addition, a high antiferromagnetic mineral concentration is inferred from $IRM_{0.1T}/IRM_{2T}$ in unit GI (Fig. 6c), where the ferrimagnetic mineral concentration is low. Values of this ratio from ~0.8–0.9 in the upper units could indicate lower high coercivity mineral concentration, with respect to unit GI. However, the goethite G proxy (Fig. 6e) varies along the entire profile, with maximum goethite concentration in the middle of subunit GIIb. Differences between the proxies may be due to $IRM_{0.1T}/IRM_{2T}$ underestimating the high coercivity content (e.g. Roberts et al., 2020).

Antiferromagnetic hematite and goethite are often closely associated in soils formed in warmer regions. Their competing formation processes depend on environmental factors, such as soil temperature and moisture, pH, rate of Fe release or organic matter (Schwertmann, 1971, 1988), and hence can record climatic information. The proportions and genetic relationship of pedogenic hematite, goethite and maghemite is an open issue for red Mediterranean soils (e.g. Barron and Torrent, 2002; Torrent et al., 2010a, b; Liu et al., 2010, 2016). The origin of the fine-grained antiferromagnetic minerals at the Galería site is not clear. They could be of detrital origin and come from surrounding soils (detrital or formed by pedogenic processes) or of authigenic origin related to pedogenesis in the cave and possibly activated by direct insolation. The positive trend between pedogenic magnetite/maghemite (identified by χ_{fd} and SP_{LC}) and fine-grained hematite and/or goethite (identified by SP_{HC}) (Fig. S4; Supplement 2) supports a pedogenic origin of these minerals (cf. Balsam et al., 2004; Torrent et al., 2006, 2010a, 2010b). Additional experiments are necessary to separate SP goethite and hematite contributions and to explain their formation mechanism.

5.2 Paleoenvironment and climatostratigraphical correlation

Our high-resolution environmental magnetic record provides a climatostratigraphical subdivision and paleoenvironmental correlation for the Galería site. In Fig. 8, low field magnetic susceptibility and goethite content are correlated with the terrestrial biosilica record from Lake Baikal (Prokopenko et al., 2006) and the global marine benthic stable $\delta^{18}O$ stack (LR04) of Lisiecki and Raymo (2005). Field observations, abruptly changing magnetic proxies and age data (Falguères et al., 2013; Demuro et al., 2014) require a substantial sedimentation hiatus in the lowermost part of the profile between units GIa and GIb because the Matuyama-Brunhes Boundary (MBB at 770.2 ± 7.3 ka; Suganuma et al., 2015) was observed between units GIa and GIb in the Galería Complex (Pérez-González et al., 2001), whereas the luminescence age in GIb is much younger (350 - 400 ka) (Falgueres et al., 2013; Demuro et al., 2014).

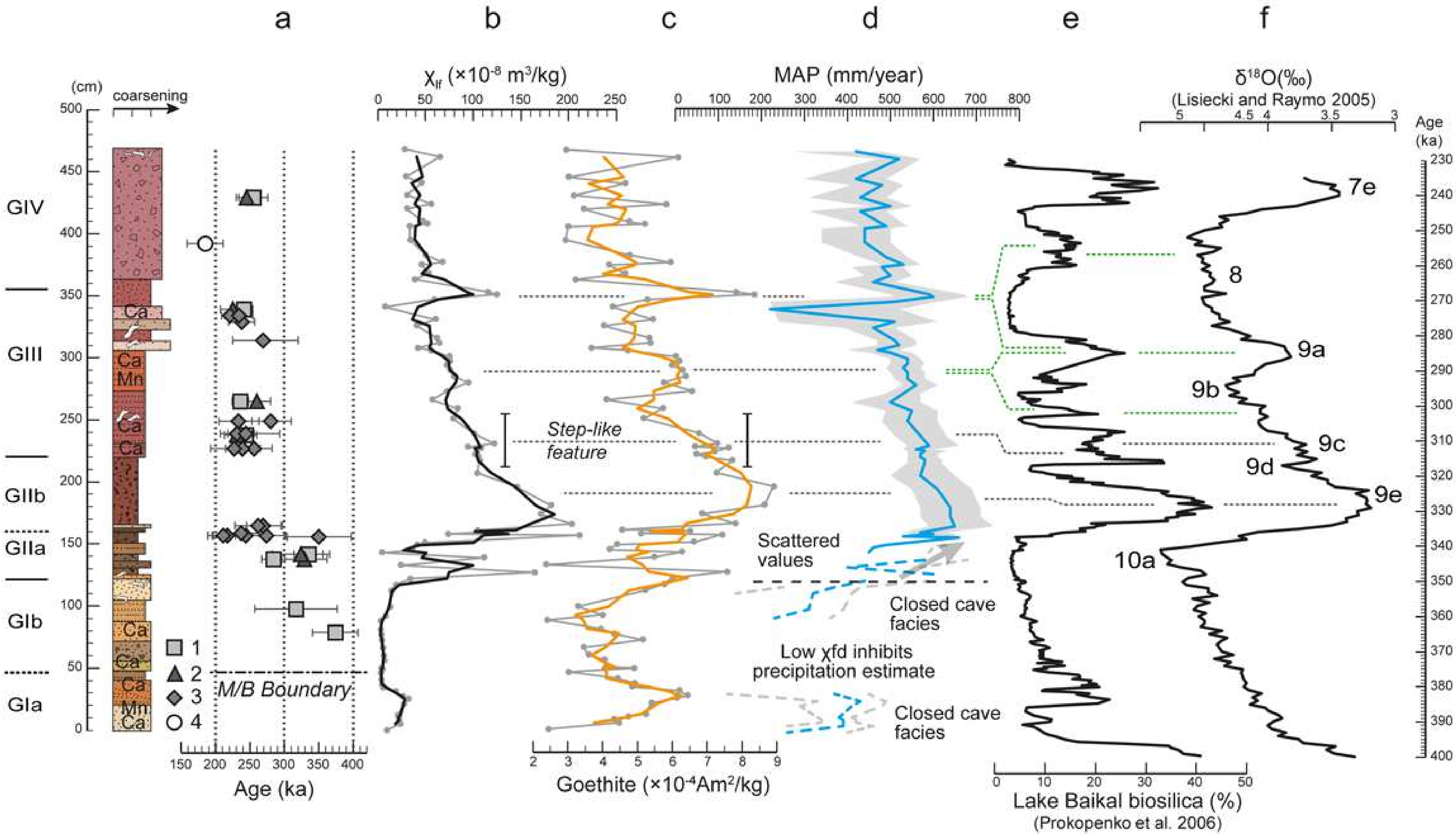

a
b
c
d
e
f
(cm)
coarsening
GIV
GIII
GIIb
GIIa
GIb
GIa
Ca
Mn
1
2
3
4
M/B Boundary
Age (ka)
χlf (×10-8 m3/kg)
Step-like feature
Goethite (×10-4Am2/kg)
MAP (mm/year)
Scattered values
Closed cave facies
Low χfd inhibits precipitation estimate
Closed cave facies
Lake Baikal biosilica (%)
(Prokopenko et al. 2006)
δ18O(‰)
(Lisiecki and Raymo 2005)
Age (ka)
7e
8
9a
9b
9c
9d
9e
10a

Figure 8. Climatostratigraphical correlation of rock magnetic and paleoenvironmental proxies. a) Age-height model including absolute data by Grün and Aguirre (1987), Falguères (1986, 2013), Berger et al. (2008) and Demuro et al. (2014). Symbol numbers refer to various dating techniques such as 1: single-grain TT-OSL, 2: pIR-IR_{225}, 3: ESR/U-series on fossil teeth, and 4: IRSL; b) low field magnetic susceptibility, χ_{lf}; c) total goethite content, G; d) MAP using the climofunction of Maher and Possolo (2013). The shaded grey area indicates 95% confidence bounds. Dashed lines for confidence bounds indicate poorly constrained intervals due to weak susceptibility and heterogeneous material (GI, closed cave) with low reliability. Maximum and minimum uncertainty values outside the Maher and Possolo (2013) climofunction are omitted (for details see Supplement 2); e) Lake Baikal biogenic silica record (Prokopenko et al., 2006); and f) marine benthic oxygen isotope stack $\delta^{18}O$ between 400 and 230 ka (Lisiecki and Raymo, 2005). Green dashed lines indicate the possible way of correlations between the upper sections of the applied environmental magnetic proxies and globally used records (for more information please see the text).

Sandy unit GIa represents an interior cave facies in which the sediment has been transported by water through the cave system (Pérez-González et al., 1995). The coarser sand points to intensified surface erosion and transportation probably due to increased precipitation and decreasing vegetation cover. Along with surface erosion, the presence of fine-grained goethite may also indicate a humid environment (Schwertmann, 1971; Cornell and Schwertmann, 2003). Unit GIb is characterized by extremely low magnetite but relatively high goethite concentration. The unit generally has low magnetic mineral concentrations. The fluctuating goethite values may be due to alternating humid and dry periods. The sedimentary environment of unit GIb is described as a closed-cave facies with a thin and discontinuous bat guano horizon (Pérez-González et al., 1995). Demuro et al. (2014) dated the sediment (374±33 ka) and a speleothem fragment (318±60 ka) in unit GIb. Based on the age results and its stratigraphic position the unit is most likely dated back to MIS10.

Susceptibilities χ_{lf} and χ_{fd} of unit GIIa follow the alternating water-lain yellow sandy silt and red clay laminae (i.e. deposited by sheet wash or in a temporary cave pond) of the unit and were possibly triggered by heavy rainfall events. Higher χ_{fd} peaks are related to redeposited soil laminae. The appearance of these sediments is ascribed to the cave ceiling collapse, which might have introduced increased surface material into the cave. Intensive precipitation and pedogenesis (Fig. 8) is attributed to a more humid and moderate environment at the MIS10/MIS9 transition (and early MIS9), as defined by the age dating. Waterlogged ground conditions are supported by palynomorph studies of Expósito et al. (2017).

The intermittent guano at the GIIa/GIIb boundary provides evidence of a relatively stable sedimentary environment without erosion. The transition from a dry to a more humid period is documented by the gradual change from silt to the overlying red clay horizon. Enhanced susceptibility and other concentration dependent magnetic parameters indicate increasing surface pedogenesis. Micromorphological studies of Vallverdú i Poch (2017) recognized mollisol complexes in unit GIIa with characteristic analogues to Mediterranean *terra rossa* soils that form in humid climates with forest vegetation. In contrast, Expósito et al. (2017) emphasize an open habitat as characteristic of the paleoenvironment.

The red clay of unit GIIb, which has high χ_{lf}, χ_{fd} and G, indicates that intense pedogenesis occurred on the surface and that mineral neoformation may have occurred in the cave, which we interpret to have been fostered by solar irradiation onto exposed surfaces under the collapsed ceiling. The age data of Demuro et al. (2014) connect the intense pedogenesis and the magnetic parameter peaks to MIS9e, the climax of this interglacial. Polygonal patterns observed in the uppermost red clay are represented by a step in χ_{fd} and G curves (ca. 220-250 cm; Fig. 8). The decreasing magnetic intensities and step-like features may be related either to aridification or seasonal wetting/drying during MIS9 (Fig. 8). Short arid (less humid) periods may have been followed by intensified precipitation, which led to surface erosion and increasing surface material infiltration through the extended ceiling hole forming the red clay horizon with massive limestone clasts. The step-like feature [ca. 220–250 cm] followed by a peak [ca. 250–300 cm] (Fig. 8) may represent a drier and a more humid period during the second part of MIS9. The step-like feature would represent MIS9d (arid) and MIS9c and the peak would represent MIS9a (for some additional information about the correlation of the peaks located between MIS9c and a, please see the text below). The magnetic parameter peaks correspond to the vertisol, inceptisol and entisol complex of Vallverdú i Poch (2017) in unit GIIb. Vertisol formation is favoured by semi-arid to sub-humid Mediterranean climates, with alternating wet and dry seasons (development of polygonal structures) and characteristic vegetation, such as savanna, natural grassland and/or woodland.

Unit GIII and the uppermost unit GIV consist of a finer grained sedimentary matrix, fine laminated horizons, fine-grained pebbles and debris possibly transported and deposited by sheet-wash processes and also rock fragments probably falling from the collapsed ceiling. χ_{lf} and G decrease gradually (Fig. 6a, e and 8b, c) thus, reflecting a transition from a humid period (e.g. MIS9 interglacial) to a drier glacial phase (e.g. MIS8 glacial). The peak around the boundary between units GIII and GIV can be connected to a shorter interglacial phase, e.g. MIS9a, or an interstadial during MIS8. Expósito et al. (2017) suggested mildly alternating steppe/Mediterranean climate during GIV. In agreement with Vallverdú i Poch (2017), the (slight) increase of SP components and goethite content indicate weak pedogenic activity (Fig. 8).

5.3 Goethite proxy

Numerous studies have used diffuse reflectance spectroscopy to determine the hematite-goethite ratio in various sediment successions, such as loess (Liu et al., 2007; Torrent et al., 2007; Hao et al., 2009; Hu et al., 2013) and Mediterranean soils (Torrent et al., 2006, 2010a and b; Liu et al., 2010). These studies developed a commonly used climate proxy related to the ratio of hematite and the sum of hematite and goethite content (Hm/[Hm+Gt]) of sediments (e.g. Torrent et al., 2007; Balsam, 2004; Long et al., 2011, 2016). The suggested reflectance parameters together with magnetic parameters, such as the ratio between hematite and pedogenic ferrimagnetic content (Hm/χ_{fd}), have been used directly or indirectly as paleoenvironmental proxies. Torrent et al. (2006, 2010a, 2010b) found large amounts of goethite (usually higher than the hematite content) in Spanish soils. Although hematite seems to be present in virtually all Galería samples, we conclude that hematite plays a less important role as a paleoclimatic proxy in our cave sequence than goethite. Therefore, we concentrate on the identification of goethite and test its reliability as a paleoclimatic proxy.

Along with the commonly used magnetic susceptibility proxy, the goethite proxy can play an important role in identifying climate fluctuations in regions with a Mediterranean climate. Its sensitivity can be traced to common processes in Mediterranean soils, such as rubefaction i.e. reddening due to hematite formation (Kämpf and Schwertmann, 1983). Previous studies (e.g. France and Oldfield, 2000; Bógalo et al., 2001; Maher et al., 2004; Hao et al., 2009; Torrent et al., 2010a, 2010b; Liu et al., 2010, 2012b; Jordanova, 2016) and our results indicate that goethite and hematite co-occur in various soils and sediment sequences. The studies of Schwertmann (1971, 1988) and Cornell and Schwertmann (2003) suggest that goethite and hematite formation (and their alteration with respect to each other) requires appropriate environmental conditions, including temperature, humidity, pH, hydrological conditions (e.g. free drainage), Fe release rates and organic matter contents. Factors in addition to humidity favour the formation of goethite over hematite. According to Cornell and Schwertmann (2003), there are two key factors for the goethite/hematite formation/alteration: temperature and pH. Goethite formation prefers relatively low temperature (below 15 °C) and low pH (i.e. more acidic environments). The cave environment seems to fulfil these two key conditions and provides favourable conditions for goethite formation. The Atapuerca archeological site is located at relatively high altitude (1085 masl) and with relatively low annual average temperatures. At present, MAT is 9.9 °C and the estimated MAT for MIS9 is between 12.7 ± 1.3 °C and 11.3 ± 2.1 °C (Blain et al., 2018). Low pH (below ~ pH 5) reduces hematite formation significantly. A more acidic environment during Galería cave sedimentation could be achieved by i) formation of carbonic acid when groundwater migrates through the limestone and ii) pedogenic organic acid infiltration from surface soils and soil units in the cave sequence. Organic material may also favour goethite formation instead of hematite (Schwertmann, 1971). Expósito et al. (2017) identified higher but irregular charcoal concentration values in samples from units GII and GIII, with highest values at the top of GIIa, which correlate with the goethite curve (Fig. 8c). Goethite variability in the Galeria succession has been compared and correlated with marine oxygen isotope stages as follows: unit GIIa represents MIS10/MIS10-9, lower unit GIIb correlates with MIS9e, upper unit GIIb formed during MIS9d–c, lower unit GIII represents MIS9a–c and the GIII/GIV boundary is correlated with the MIS9a or MIS8 interstadials (Fig. 8). There remains some uncertainty in the chronostratigraphical correlation of the section with the global records, especially in the upper part of unit GIII and at the boundary GIII/IV. The increasing goethite content in the upper part of unit GIII may relate to a weak pedogenic period at the end of MIS9 (c or a), and the peak at the boundary GIII/IV may represent a shorter warm period in MIS9 (MIS9a) or an interstadial during MIS8 (Fig. 8).

We suggest the following model for goethite formation in the Galería succession. Although calcareous rocks in general are not rich in iron minerals, there are multiple sources which provide resources for goethite formation during the development of the Galería succession. Atmospheric dust, various clastic sedimentary rocks in the vicinity of the profile (Pérez-González et al., 1995) and the paleosols on the surface may contain silicate minerals (e.g. phyllosilicates) which can be the source of iron during goethite forming.

Interglacial periods had relatively high temperatures, although lower temperatures will be observed for the cave than the surface due to the higher altitude site and largely reduced insolation. The interglacial climate favoured intense pedogenesis, which led to increased organic acid infiltration via precipitation into the cave system. In general, the pH range in the surroundings is between 5.5 and 7.5 (Calvo de Anta et al., 2020) and the estimated average pH in temperate Mediterranean soils based on the European topsoil database survey (LUCAS) is 6.7 (Jones et al., 2015). Along with carbonic acid, organic acids would have lower the pH significantly to 4-5, thus fostering goethite formation. In glacial periods, colder temperatures generally favour goethite formation, although due to the lack of intense pedogenesis (less organic acid and organic material formation), goethite formation was reduced compared to interglacial periods.

5.4 Reconstruction of surface annual precipitation

Pedogenic magnetite/maghemite production depends largely on precipitation (MAP) (e.g. Heller et al. 1993; Maher et al., 1994, 2002; Maher and Possolo, 2013; Panaiotu et al., 2001; Geiss et al., 2008; Balsam et al., 2011; Bradák et al., 2011; Maxbauer et al., 2016b; Ahmed and Maher, 2018; Gao et al., 2019). The occurrence of several relict/reworked soil horizons in the Galería Complex (Valverdú i Poch, 2017) and the demonstrated SP mineral assemblages are used here to estimate the annual (paleo)precipitation on the land surface (Fig. 8d). The paleoprecipitation curve in Fig. 8d was constructed using the climofunction of Maher and Possolo (2013), which describes the relationship between MAP and χ_{fd} in paleosols on the Chinese Loess Plateau and the Russian steppe. We have chosen this climofunction because the pedogenic susceptibility of Spanish river terrace soils studied by Bógalo (1999) fits the Maher and Possolo (2013) climofunction reasonably well. In addition, the fermentation process proposed by Barrón and Torrent (2002) and Torrent et al. (2006, 2010a, b) to explain the magnetic enhancement in Spanish Mediterranean soils has also been applied to Chinese loess-paleosol systems (e.g. Liu et al, 2007; Hao et al., 2009; Torrent et al., 2007; Zhao et al., 2017), so it could also apply to pedogenic magnetite formation in the Galería Complex.

Assessment of uncertainties for MAP estimation is important for quantitative paleoclimatic interpretations (Heslop and Roberts, 2013). Each sedimentary unit (GI to GIV) was divided into subunits that consider pedological and physical macroscopical characteristics, grain size, debris occurrence and Munsell colour (Supplement 1) to evaluate the MAP uncertainty (cf. Supplement 2 for detailed MAP reconstruction). Probable *in situ* mineral neoformation by solar irradiation may also give rise to different precipitation estimates. Therefore, we calculated MAP for samples that originate from the same stratigraphic unit (GIIb) but are displaced horizontally (GH horizon, Fig. 2). Although the difference between the calculated MAP for one sample that was not exposed to solar irradiation (600 + 20/-undetermined mm/year) and for another sample that was probably exposed to the sun (680 ± 70 mm/year) is small, the observed data trend suggests increased syn-depositional mineral neoformation under solar irradiation. Slightly intensified MAP values (by ~10%) might, therefore, be expected for the potentially irradiated sample sections C-D, whereas sections E and F were always in shade (cf. Fig. 2).

5.5 Annual precipitation at Galería during MIS9 and MIS8

Lower unit GIIa (122-145 cm) has scattered MAP values between 400 and 620 mm/year (Fig. 8d). However, uncertainty (~120 mm/year) is high (Fig. 8d; dotted line) and related to the character of the material (laminated sediment); therefore, these paleoprecipitation data should be treated with caution. Slightly higher and less scattered MAP values of 490-660 ± 120 mm/year are reconstructed in uppermost part of GIIa (150-160 cm). We propose the following scheme to describe the "extreme" precipitation differences observed in GIIa. The higher annual mean paleoprecipitation in GIIa of 620-660 mm/year may represent an interglacial or warmer interstadial when pedogenesis was enhanced during an earlier warm phase than MIS9. The remains of such paleosols (representing high precipitation) were mixed and are preserved together with their parent material (represented by low precipitation) by redeposition before MIS9. Estimated 650-570 ± 60 mm/year MAP values during MIS9e (GIIb) are similar to those of the preceding interglacial (older than MIS9), which is preserved in the redeposited material of GIIa and are similar to recent precipitation (646 mm/year in Atapuerca village, AEMET, 2019) and lower than the estimates of Blain et al. (2018). The environmental magnetic parameters of GIIb indicate a strong interglacial period, most likely MIS9e, which was assigned a strong interglacial by Past Interglacials Working Group of PAGES (2016).

The potential remains of a weakly developed soil in unit GIII suggested by Vallverdú i Poch (2017) are correlated with MIS9c (or a, see above at 5.3) with an estimated 530-560 ± 40 mm/year MAP (Fig. 8d). These slightly lower values than in peak MIS9e indicate a drier pedogenic environment and are consistent with development of a weaker paleosol. The minimum precipitation estimated at the end of MIS9 is characteristic of drier Mediterranean or continental areas, and the gradual aridification possibly indicates the transition toward the MIS8 glacial. The magnetic peaks at the boundary between units GIII and GIV may be due to a shorter warm phase at the end of MIS9 interglacial (MIS9a) or a relatively humid (600 ± 90 mm/year) period during MIS8. The reconstructed MAP at 420-520 ± 70 mm/year in unit GIV is lower than the recent annual precipitation in Atapuerca village.

5.6 Global and regional (Iberian) paleoclimate during MIS9 and MIS8

Following the observations, assignments and schemes of Lang and Wolff (2011) for glacial periods and the Past Interglacials Working Group of PAGES (2016) interglacial periods, the global climate trends during MIS9 and 8 can be summarized as follows. Based on climate proxies from Antarctica, the SW Pacific, eastern equatorial Pacific and North Atlantic oceans and from ice core CH4, MIS9e seems to be the strongest interglacial among those of the past 800 ka (Past Interglacials Working Group of PAGES, 2016). In contrast, most terrestrial records document contrasting patterns compared to marine and ice core proxies. Key paleoclimatic records, such as arboreal pollen from Tenaghi Philippon (Tzedakis et al., 2006), biogenic silica from Lake Baikal (Prokopenko et al., 2006) and Si/Ti from Lake El´gygytgyn (Melles et al., 2012) and Xifeng loess (Guo et al., 2009), indicate a strong interglacial in MIS11c but a slightly weaker MIS9e. In most of these suggested records, MIS11 is one of the most intense interglacials among the interglacials in the last 800 ka. MIS9e is a warm and intense interglacial (if not one of the most intense) in the Middle and Late Pleistocene (Past Interglacials Working Group of PAGES, 2016). MIS8 does not have strong and intense glacial characteristics among the glacials of the last 800 ka (Lang and Wolff, 2011).

Reconstructed paleoprecipitation values and characteristic paleoclimatic proxy peaks, such as magnetic susceptibility and the goethite proxy (χ_{lf} and G), from the Galería Complex are consistent with global tendencies and indicate an intense MIS9 interglacial. Our paleoprecipitation estimates from the Galeria succession do not change abruptly but rather decrease smoothly from MIS9 to MIS8 (Fig. 8), thus mimicking the global climate change.

In a regional context, the reconstructed slightly higher Galeria precipitation during MIS9 is lower than that of Blain et al. (2018) (ca. 800-1000 mm MAP). Blain et al. (2018) suggested a slightly cooler MIS9 compared to MIS11c, but a warmer and more humid climate compared to the present-day regional climate. Our results do not indicate such differences between MIS9 and the present day. During MIS8, a MAP value of 460 ± 70 mm/year is reconstructed for the Galería Complex. It has an opposite tendency compared to results from eastern and central Spain. Although there have been only a few Iberian MIS8 paleotemperature and precipitation estimates, Blain et al. (2017, 2018) suggested that colder (ΔT: -2.2-2.5 ºC) and wetter (ΔMAP: +291.9 and +282.3 mm) conditions occurred in Eastern Spain and that cooler and moister conditions with total rainfall higher than present occurred in central Spain.

Along with such paleoclimatic information, Roucoux et al. (2006) reconstructed details of MIS9 to MIS7 environments for the Southwestern Iberian Peninsula. They identified the most extreme glacial conditions during early MIS8, which was followed by a warmer, interstadial period (~263 ka). This warmer period might also be observed in the climate proxies from the Galería Complex (Fig. 8). Characteristic peaks are found in the magnetic susceptibility, goethite and MAP curves at the boundary of units GIII and GIV (~350 cm; Fig. 8), which possibly represent the warmer MIS8 as suggested by Roucoux et al. (2006).

6. Conclusions

Detailed rock magnetic studies have enabled identification of environmentally sensitive fine-grained ferrimagnetic minerals (magnetite/maghemite) across a well-developed 5m thick section of cave sediments in the Galería Complex, Atapuerca archeological site (Northern Spain), which consists of four major sedimentation units (GI – GIV). The highest magnetite concentration, most likely of pedogenic origin, appears in unit GIIb. Solar irradiation introduced through the ceiling opening to the cave possibly favoured intermittent wetting and drying conditions of the cave sediment and fostered authigenic SP ferrimagnetic particle formation by a fermentation process. Single domain and superparamagnetic goethite and hematite are also identified. Some magnetic proxies (e.g. goethite content G) based on IRM experiments at room and liquid nitrogen temperature provide estimates of the stratigraphic distribution of goethite. They indicate maximum goethite concentration also in the middle of unit GIIb, at ~300 ka.

The goethite content is a key proxy for climato-stratigraphic correlation in the Galeria Complex. Its formation was favoured over that of hematite because cave sedimentation took place under cooler temperatures (due to higher altitude and subsurface formation) and acidic pH conditions (decreasing pH due to carbonic and organic acids). The goethite proxy and the commonly used magnetic susceptibility proxy work well (Fig. 8) when correlating the Galería profile with other global paleoclimatic proxies. The luminescence-dated (Demuro et al., 2014) magnetic proxies correlate positively with marine $\delta^{18}O$ stages and with some substages, which gives new insights for Iberian Middle Pleistocene terrestrial paleoclimate reconstructions.

Reconstructed paleoclimatic trends and paleoprecipitation are consistent with global tendencies but also record regional differences. Paleoprecipitation estimates indicate a humid climate similar to present-day conditions for the MIS9 interglacial (~650 mm/year maximum annual precipitation), which changed gradually to a mild and only slightly cooler and less humid (420 to 520 mm/year) MIS8 glacial period. This mild glacial might be interrupted once by a warmer interstadial period. The magnetic MAP estimates from the Galería Complex result in significantly lower values compared to previous paleoprecipitation for the Iberian Peninsula during MIS9 and MIS8.

Acknowledgements

This work was supported by the Junta de Castilla y León (Spain) and the European Regional Development Fund (ERDF) (BU235P18) and the research projects CGL2016-77560-C2, CGL2018-093925-B-C31, and CGL2017-89603-R of the Spanish Ministry of Science and

Innovation and PID2019-108753GB-C21 and PID2019-105796GB-I00 of the Spanish State Research Agency (AEI/10.13039/501100011033) and FEDER funding (European Union). B. Bradák acknowledges financial support from project BU235P18 (Junta de Castilla y León, Spain) and the European Regional Development Fund (ERD). M. Calvo-Rathert acknowledges funding from the Fulbright Commission and the Spanish Ministry of Science Innovation and Universities for a research stay at University of Hawaii at Manoa. We thank A. Lorente (Universidad de Burgos) for her assistance with calculating paleoprecipitation uncertainties, the Atapuerca Research Team (EIA) and the Fundación Atapuerca for continuous support of this research, particularly I. Cáceres, coordinator of the Galería site, Raquel Pérez and J. Valverdú for their work in the field and A. Pérez-González for providing help in the early stages of this project and A. Roberts and an anonymous reviewer for constructive comments that helped to improve the manuscript.

References

Agencia Española de Metorología (AEMET), 2019. Climate Atlas Viewer of the Peninsula and Balearic Islands. http://www.aemet.es/en/serviciosclimaticos/datosclimatologicos/atlas_climatico/visor_atlas_climatico (accessed 9 December 2019)

Ahmed, I.A.M., Maher, B.A., 2018. Identification and paleoclimatic significance of magnetite nanoparticles in soils. Proc. Natl. Acad. Sci. U. S. A. 115, 1736–1741. https://doi.org/10.1073/pnas.1719186115

Arsuaga, J.L., Bermudez de Castro, J.M. and Carbonell, E. (Eds.) 1997. The Sima de los Huesos Hominid site. J. Hum. Evol., 33 (2–3), 105–421. https://doi.org/10.1006/jhev.1997.0169

Arsuaga, J.L., Gracia, A., Lorenzo, C., Martínez, I., Pérez, P.J., 1999. Resto craneal humano de Galería / cueva de Zarpazos (Sierra de Atapuerca, Burgos), in: Carbonell, E., Rosas, A., Díez, J.C (Eds.), Atapuerca: Ocupaciones humanas y paleoecología del yacimiento de Galería. Arqueología en Castilla y León, Memorias 7, pp. 233–235.

Arsuaga, J.L., Martínez, I., Arnold, L.J., Aranburu, A., Gracia, A., Sharp, W.D., Quam, R.M., Falguères, C., Pantoja, A., Bischoff, J., Poza, E., Parés, J.M., Carretero, J.M., Demuro, M., Lorenzo, C., Sala, N., Martinón, M., García, N., Alcázar, A., Cuenca, G., Gómez, A., Moreno, D., Pablos, A., Shen, C.C., Rodríguez, L., Ortega, A.I., García, R., Bonmatí, A., Bermúdez de Castro, J.M., Carbonell, E. 2014. Neandertal roots: Cranial and chronological evidence from Sima de los Huesos. Science 344, 1358–1363. https://doi.org/10.1126/science.1253958

Balsam, W., Ji, J., Chen, J., 2004. Climatic interpretation of the Luochuan and Lingtai loess sections, China, based on changing iron oxide mineralogy and magnetic susceptibility. Earth Planet. Sci. Lett. 223 (3–4), 335–348. https://doi.org/10.1016/j.epsl.2004.04.023

Balsam, W.L., Ellwood, B.B., Ji, J., Williams, E.R., Long, X., El Hassani, A., 2011. Magnetic susceptibility as a proxy for rainfall: Worldwide data from tropical and temperate climate. Quat. Sci. Rev. 30, 2732–2744. https://doi:10.1016/j.quascirev.2011.06.002

Banerjee, S.K., Hunt, C.P., Liu, X.M., 1993. Separation of local signals from the regional paleomonsoon record of the Chinese Loess Plateau: a rock-magnetic approach. Geophys. Res. Lett. 20, 843–846. https://doi.org/10.1029/93GL00908

Barrón, V., Torrent, J., 2002. Evidence for a simple pathway to maghemite in Earth and Mars soils. Geochim. Cosmochim. Acta 66(15), 2801–2806. https://doi.org/10.1016/S0016-7037(02)00876-1

Bella, P., Bosák, P., Braucher, R., Pruner, P., Hercman, H., Minár, J., Veselský, M., Holec, J., Léanni, L., 2019. Multi-level Domica–Baradla cave system (Slovakia, Hungary): Middle Pliocene–Pleistocene evolution and implications for the denudation chronology of the Western Carpathians. Geomorphology 327, 62–69. https://doi.org/10.1016/j.geomorph.2018.10.002

Benito-Calvo, A., Ortega, A.I., Pérez-González, A., Campaña, I., Bermúdez de Castro, J.M., Carbonell, E., 2017. Palaeogeographical reconstruction of the Sierra de Atapuerca Pleistocene sites (Burgos, Spain). Quat. Int. 433, 379–392. https://doi.org/10.1016/j.quaint.2015.10.034

Benito-Calvo, A., Pérez-González, A., Parés, J.M. 2008. Quantitative reconstruction of Late Cenozoic landscape: a case study in the Sierra de Atapuerca (Burgos, Spain). Earth Surf. Proc. Land. 33, 196–208. https://doi.org/10.1002/esp.1534

Berger, G.W., Pérez-González, A., Carbonell, E., Arsuaga, J.L., Bermúdez de Castro, J.M., Ku, T.L., 2008. Luminescence chronology of cave sediments at the Atapuerca paleoanthropological site, Spain. J. Hum. Evol. 55, 300–311. https://doi.org/10.1016/j.jhevol.2008.02.012

Bermúdez de Castro, J.M., Arsuaga, J.L., Carbonell, E., Rosas, A., Martínez, I., Mosquera, M., 1997. A hominid from the Lower Pleistocene of Atapuerca, Spain: possible ancestor to Neandertals and modern human. Science 276, 1392–1395. https://doi.org/10.1126/science.276.5317.1392

Bermúdez de Castro, J.M., Martinón-Torres, M., Robles, A.G., Prado, L., Carbonell, E., 2010. New human evidence of the Early Pleistocene settlement of Europe, from Sima del Elefante site (Sierra de Atapuerca, Burgos, Spain). Quat. Int. 223–224, 431–433. https://doi.org/10.1016/j.quaint.2009.07.024

Bermúdez de Castro J.M., Martinón-Torres M., 2013. A new model for the evolution of the human Pleistocene populations of Europe. Quat. Int. 295, 102-112. https://doi.org/10.1016/j.quaint.2012.02.036

Blain, H.-A., Ruiz Zapata, M.B., Gil García, M.J., Sese, C., Santonja, M., Perez-Gonzalez, A., 2017. New palaeoenvironmental and palaeoclimatic reconstructions for the Middle Palaeolithic site of Cuesta de la Bajada (Teruel, eastern Spain) inferred from the amphibian and squamate reptile assemblages. Quat. Sci. Rev. 173, 78-91. https://doi.org/10.1016/j.quascirev.2017.08.019

Blain, H-A., Silva, J. A. C., Arenas, J. M. J., Margari, V., Roucoux, K. 2018. Towards a Middle Pleistocene terrestrial climate reconstruction based on herpetofaunal assemblages from the Iberian Peninsula: State of the art and perspectives. Quat. Sci. Rev. 191, 167–188. https://doi.org/10.1016/j.quascirev.2018.04.019

Bógalo, M.F., 1999. Propiedades magnéticas de los suelos de los piedemontes plio-pleistocenos y de las terrazas fluviales cuaternarias del centro de la Península Ibérica. Implicaciones paleoambientales. PhD thesis. Complutense Univ. Madrid, Spain. CD-ROM edition. ISBN: 84-669-1563-X.

Bógalo, M.F., Heller, F., Osete, M.L., 2001. Isothermal remanence experiments at room and at liquid nitrogen temperature: Application to soil studies. Geophys. Res. Lett. 28, 419–422. https://doi.org/10.1029/2000GL012032

Bosák, P., Pruner, P., 2011. Magnetic record in cave sediments: A review, in: The Earth's Magnetic Interior. Eds. Petroský, E., Ivers, D., Harinarayana, T. and Herrero-Bervera, E., pp. 343–360, IAGA Special Sopron Book Series, Springer.

Bradák, B., Thamó-Bozsó, E., Kovács, J., Márton, E., Csillag, G., Horváth, E., 2011. Characteristics of Pleistocene climate cycles identified in Cérna Valley loess-paleosol section (Vértesacsa, Hungary). Quat. Int. 234, 86–97. https://doi.org/10.1016/j.quaint.2010.05.002

Calvo de Anta, R., Luís, E., Febrero-Bande, M., Galiñanes, J., Macías, F., Ortíz, R., Casás, F., 2020. Soil organic carbon in peninsular Spain: Influence of environmental factors and spatial distribution. Geoderma 370, 114365. https://doi.org/10.1016/j.geoderma.2020.114365

Carbonell, E., Bermúdez de Castro, J. M., Arsuaga, J.L., Díez, J.C., Rosas, A., Cuenca-Bescós, G., Sala, R., Mosquera, M., Rodríguez, X.P., 1995. Lower Pleistocene Hominids and Artifacts from Atapuerca-TD6 (Spain). Science 296, 826-828.2014. https://science.sciencemag.org/content/269/5225/826

Carbonell, E., Bermúdez de Castro, J.M., Parés, J.M., Pérez-González, A., Cuenca-Bescós, G., Ollé, A., Mosquera, M., Huguet, R., van der Made, J., Rosas, A., Sala, R., Vallverdú, J., García, N., Granger, D.E., Martinón-Torres, M., Rodríguez, X.P., Stock, G.M., Vergès, J.M., Allué, E., Burjachs, F., Cáceres, I., Canals, A., Benito, A., Díez, C., Lozano, M., Mateos, M., Navazo, M., Rodríguez, J., Rosell, J. and Arsuaga, J.L., 2008. The first hominin of Europe. Nature 452, 465–470. https://doi.org/10.1038/nature06815

Carbonell, E., Cáceres, I., Lozano, M., Saladié, P., Rosell, J., Lorenzo, C., Vallverdú, J., Huguet, R., Canals, A., Castro, J.M.B. De, 2010. Cultural cannibalism as a paleoeconomic system in the European lower pleistocene. Curr. Anthropol. 51, 539–549. doi:10.1086/653807

Carbonell, E., Rosas, A., Díez, J.C. (Eds.), 1999. Atapuerca: Ocupaciones humanas y Paleoecología del yacimiento de Galería. Arqueología en Castilla y León, Junta de Castilla y León, Memorias 7, 390 p.

Carracedo, J.C., Heller, F., Soler, V., Aguirre, E., 1987. Estratigrafía magnética del yacimiento de Atapuerca: determinación del límite Matuyama/Bruhnes. In: Aguirre, E., Carbonell, E., Bermúdez de Castro, J.M. (Eds.), El Hombre fósil de Ibeas y el Pleistoceno de la Sierra de Atapuerca, Junta de Castilla y León, pp. 193–199.

Carrancho, Á., Villalaín, J.J., Vergès, J.M., Vallverdú, J., 2012. Assessing post-depositional processes in archaeological cave fires through the analysis of archaeomagnetic vectors. Quat. Int. 275, 14–22. https://doi.org/:10.1016/j.quaint.2012.01.010

Cornell, R.M., Schwertmann, U., 2003. The Iron Oxides: Structure, Properties, Reactions, Occurrences and Uses, 2nd ed, Wiley-VCH., 664 p.

Cuenca-Bescos, G., Melero-Rubio, M., Rofes, J., Martinez, I., Arsuaga, J.L., Blain, H-A., Lopez-Garcia, J.M., Carbonell, E., Bermudez de Castro, J.M., 2011. The Early-Middle Pleistocene environmental and climatic change and the human expansion in Western Europe: A case study with small vertebrates (Gran Dolina, Atapuerca, Spain). Journal of Human Evolution 60, pp. 481-491. http://dx.doi.org/10.1016/j.jhevol.2010.04.002

Dearing, J.A., Dann, R.J.L., Hay, K., Less, J.A., Loveland, P.J., Maher, B.A., O'Grady, K., 1996a. Frequency-dependent susceptibility measurements of environmental materials. Geophys. J. Int. 124, 228–240. https://doi.org/10.1111/j.1365-246X.1996.tb06366.x

Dearing, J.A., Hay, K.L., Baban, S.M.J., Huddleston, A.S., Wellington, E.M.H., Loveland, P.J., 1996b. Magnetic susceptibility of soil: An evaluation of conflicting theories using a national data set. Geophys. J. Int. 127(3), 728–734. https://doi.org/10.1111/j.1365-246X.1996.tb04051.x

Dearing, J.A, Bird, P.M., Dann, R.J.L., Benjamin, S.F., 1997. Secondary ferrimagnetic minerals in Welsh soils: a comparison of mineral magnetic detection methods and implications for mineral formation. Geophys. J. Int. 130, 727–736. https://doi.org/10.1111/j.1365-246X.1997.tb01867.x

Demuro, M., Arnold, L.J., Parés, J.M., Pérez-González, A., Ortega, A.I., Arsuaga, J.L., Bermúdez de Castro, J.M., Carbonell, E., 2014. New luminescence ages for the Galería

Complex archaeological site: Resolving chronological uncertainties on the Acheulean record of the Sierra de Atapuerca, Northern Spain. PLoS One 9. https://doi.org/10.1371/journal.pone.0110169

Djerrab, A., Aïfa, T., 2010. Contribution of rock magnetism to stratigraphy and palaeoenvironment of the Karaïn cave infill, Antalya, Turkey. Stud. Geophys. Geod. 54, 49–76. https://doi.org/10.1007/s11200-010-0003-0

Egli, R., 2003. Analysis of the field dependence of remanent magnetization curves. J. Geophys. Res. Solid Earth 108, 1–25. https://doi.org/10.1029/2002JB002023

Egli, R., 2004. Characterization of individual rock magnetic components by analysis of remanence curves, 1. Unmixing natural sediments. Stud. Geophys. Geod. 48, 391–446. https://doi.org/10.1023/B:SGEG.0000020839.45304.6d

Ellwood, B.B., Harrold, F.B., Benoist, S.L., Straus, L.G., Gonzalez Morales, M., Petruso, K., Bicho, N.F., Zilhγo, J., Soler, N., 2001. Paleoclimate and intersite correlations from Late Pleistocene/Holocene cave sites: Results from Southern Europe. Geoarchaeology 16, 433–463. https://doi.org/10.1002/gea.1011

Evans, M.E., Heller, F., 2003. Environmental Magnetism: Principles and Applications of Enviromagnetics, Academic Press, 299 p.

Exposito, I., Burjachs F., Allue, E., 2017. Filling in the gaps: The contribution of non-pollen palynomorphs to knowledge about the local environment of the Sierra de Atapuerca caves during the Pleistocene. Quat. Int. 433, 224–242. https://doi.org/10.1016/j.quaint.2015.09.016

Falguères, C., 1986. Datations de sites acheuléens et moustériens du midi méditerranéen par la méthode de résonance de spin Electronique. Ph.D. thesis, Muséum National d'histoire naturelle, Paris.

Falguères, C., Bahain, J.-J., Bischoff, J.L., Pérez-González, A., Ortega, A.I., Ollé, A., Quiles, A., Ghaleb, B., Moreno, D., Dolo, J.-M., Shao, Q., Vallverdú, J., Carbonell, E., Bermúdez de Castro, J.M., Arsuaga, J.L., 2013. Combined ESR/U-series chronology of Acheulian hominid-bearing layers at Trinchera Galería site, Atapuerca, Spain. J. Hum. Evol. 65, 168–184. https://doi.org/10.1016/j.jhevol.2013.05.005

Falguères, C., Bahain, J.J., Yokohama, Y., Bischoff, J.L., Arsuaga, J.L., Bermudez de Castro, J.M., Carbonell, E. & Dolo, J.M., 2001. Datation par RPE et U-Th des sites pléistocènes d'Atapuerca: Sima de los Huesos, Trinchera Dolina et Trinchera Galería. Bilan géochronologique. L'Antropologie 105, 71–81. https://doi.org/10.1016/S0003-5521(01)80006-6

Fang, X.M., Li J.J., Banerjee, S.K., Jackson, M., Oches, E.A., Van der Voo, R., 1999. Millennial-scale climatic change during the last interglacial period: Superparamagnetic sediment proxy from paleosol S1, western Chinese Loess Plateau. Geophys. Res. Lett. 26, 2485-2488. https://doi.org/10.1029/1999GL008335

Ford, D.C., Williams, P.W., 2007. Karst Hydrology and Geomorphology. John Wiley & Son Ltd., 576 p.

Forster, T., Evans, M.E., Heller, F., 1994. The frequency dependence of low field susceptibility in loess sediments, Geophys. J. Int. 118, 636–642. https://doi.org/10.1111/j.1365-246X.1994.tb03990.x

France, D.E., Oldfield, F., 2000. Identifying goethite and hematite from rock magnetic measurements of soils and sediments. J. Geophys. Res. 105(B2), 2781–2795. https://doi.org/10.1029/1999JB900304

Gao, X., Hao, Q., Oldfield, F., Bloemendal, J., Deng, C., Wang, L., Song, Y., Ge J., Wu, H., Xu, B., Li, F., Han, L., Fu, Y., Guo Z., 2019. New high-temperature dependence of magnetic susceptibility-based climofunction for quantifying paleoprecipitation from

Chinese loess. Geochem., Geophys., Geosyst. 4273–4291. https://doi.org/10.1029/2019GC008401

García-Medrano, P., Cáceres, I., Ollé, A., Carbonell, E., 2017. The occupational pattern of the Galería site (Atapuerca, Spain): A technological perspective. Quat. Int. 433, 363-378. http://dx.doi.org/10.1016/j.quaint.2015.11.013

Gehring, A.U., Fischer, H., Louvel, M., Kunze, K., Weidler, P. G. 2009. High temperature stability of natural maghemite: A magnetic and spectroscopic study. Geophys. J. Int. 179(3), 1361–1371. https://doi.org/10.1111/j.1365-246X.2009.04348.x

Geiss, C.E., Egli, R., Zanner, C.W., 2008. Direct estimates of pedogenic magnetite as a tool to reconstruct past climates from buried soils. J. Geophys. Res. Solid Earth 113, 1–15. https://doi.org/10.1029/2008JB005669

Gillieson, D., 1998. Caves: Processes, Development and Management, Blackwell Publishers, 324 p.

Goldberg, P., Sherwood, S.C., 2006. Deciphering human prehistory through the geoarcheological study of cave sediments. Evolutionary Anthropology 15, 20–36. https://doi.org/10.1002/evan.20094

Grün, R., Aguirre, E., 1987. Datación por ESR y por la serie del U, en los depósitos cársticos de Atapuerca. In: Aguirre, E., Carbonell, E., Bermúdez de Castro, J.M. (Eds.), El Hombre fósil de Ibeas y el Pleistoceno de la Sierra de Atapuerca, Junta de Castilla y León, pp. 201–204.

Guo, Z. T., Berger, A., Yin, Q. Z., Qin, L. 2009. Strong asymmetry of hemispheric climates during MIS-13 inferred from correlating China loess and Antarctica ice records, Clim. Past 5(1), 21–31. https://doi.org/10.5194/cp-5-21-2009

Hajna, N.Z., Mihevc, A., Pruner, P., Bosák, P., 2010. Palaeomagnetic research on karst sediments in Slovenia. Int. J. Speleol. 39(2), 47–60. http://dx.doi.org/10.5038/1827-806X.39.2.1

Hao, Q., Oldfield, F., Bloemendal, J., Torrent, J., Guo, Z., 2009. The record of changing hematite and goethite accumulation over the past 22 Myr on the Chinese Loess Plateau from magnetic measurements and diffuse reflectance spectroscopy. J. Geophys. Res. Solid Earth, 114(12), 1–18. https://doi.org/10.1029/2009JB006604

Häuselmann, P., Mihevc, A., Pruner, P., Horáček, I., Čermák, S., Hercman, H., Sahy, D., Fiebig, M., Hajna, N.Z., Bosák, P., 2015. Snežna jama (Slovenia): Interdisciplinary dating of cave sediments and implication for landscape evolution. Geomorphology 247, 10–24. https://doi.org/10.1016/j.geomorph.2014.12.034

Heller, F., Shen, C.D., Beer, J., Liu, X., M., Liu, T.S., Bronger, A, Suter, M., Bonani, G., 1993. Quantitative estimates and palaeoclimatic implications of pedogenic ferromagnetic mineral formation in Chinese loess. Earth Planet. Sci. Letters 114, 385–390. https://doi.org/10.1016/0012-821X(93)90038-B

Helm, P., Stirling, R., Glendinning, S., 2016. The implications of using estimated solar radiation on the derivation of potential evapotranspiration and soil moisture deficit within an embankment. Procedia Eng. 143, 697–707. https://doi.org/10.1016/j.proeng.2016.06.105

Herrejón, Á., Carrancho, Á., Villalaín, J.J., Mallol, C., Hernández, C.M., 2019. An experimental approach to the preservation potential of magnetic signatures in anthropogenic fires. PLoS ONE. https://doi.org/10.1371/journal.pone.0221592

Herries, A.I.R., Shaw, J., 2011. Palaeomagnetic analysis of the Sterkfontein palaeocave deposits: Implications for the age of the hominin fossils and stone tool industries. J. Hum. Evol. 60, 523–539. https://doi.org/10.1016/j.jhevol.2010.09.001

Heslop, D., Roberts, A.P., 2013. Calculating uncertainties on predictions of palaeoprecipitation from the magnetic properties of soils. Glob. Planet. Change 110, 379–385. doi:10.1016/j.gloplacha.2012.11.013

Hewitt, G.M., 1999. Postglacial recolonization of European biota. Biol. J. Linn. Soc. 68, 87–112. https://doi.org/10.1006/bijl.1999.0332

Hrouda, F., 2011. Models of frequency-dependent susceptibility of rocks and soils revisited and broadened. Geophys. J. Int. 187, 1259–1269. https://doi.org/10.1111/j.1365-246X.2011.05227.x

Hu, P., Liu, Q., Torrent, J., Barrón, V., Jin, C., 2013. Characterizing and quantifying iron oxides in Chinese loess/paleosols: Implications for pedogenesis. Earth Planet. Sci. Lett. 369–370, 271–283. https://doi:10.1016/j.epsl.2013.03.033

Huguet, R., Cáceres, I., Díez, J.C., Rosell, J., 1999. Estudio tafonómico y zooarqueológico de la unidad G.II de Galería (Sierra de Atapuerca), in: Carbonell, E., Rosas, A., Díez, J.C, (Eds.), Atapuerca: Ocupaciones humanas y paleoecología del yacimiento de Galería, Arqueología en Castilla y León, Junta de Castilla y León, Memorias 7, pp. 245–264.

Irmak, S., Irmak, A., Allen, R.G., Jones, J.W., 2003. Solar and net radiation-based equations to estimate reference evapotranspiration in humid climates. J. Irrig. Drain. Eng. 129, 336–347. https://doi.org/10.1061/(ASCE)0733-9437(2003)129:5(336)

Jiang, Z., Liu, Q., Roberts, A.P., Barrón, V., Torrent, J., Zhang, Q. 2018. A new model for transformation of ferrihydrite to hematite in soils and sediments: Geology 46, 1–4, https://doi.org/10.1130/G45386.1

Jones, A., Fernandez-Ugalde, O., Scarpa, S., 2020. LUCAS 2015 Topsoil Survey. Presentation of dataset and results, EUR 30332 EN, Publications Office of the European Union: Luxembourg. ISBN 978-92-76-21080-1. https//doi:10.2760/616084/JRC121325

Jordanova, N., 2016. Soil magnetism. Applications in Pedology, Environmental Science and Agriculture, Academic Press, 466 p.

Kämpf, A., Schwertmann, U., 1983. Goethite and hematite in a climosequence in Sourthern Brazil and their application in classification of kaolinitic soils. Geoderma 29, 27–39. https://doi.org/10.1016/0016-7061(83)90028-9

Kean, W., Ahler, S., Fowler, M., Wolfman, D., 1997. Archaeomagnetic record from Modoc Rock Shelter, Illinois, for the time range of 6200–8900 B.P. Geoarchaeology 12, 93–115. https://doi.org/10.1002/(SICI)1520-6548(199703)12:2<93::AID-GEA1>3.0.CO;2-3

Lagroix, F., Guyodo, Y., 2017. A new tool for separating the magnetic mineralogy of complex mineral assemblages from low temperature magnetic behavior. Front. Earth Sci. 5, 1–11. https://doi.org/10.3389/feart.2017.00061

Lang, N., and Wolff, E.W. 2011. Interglacial and glacial variability from the last 800 ka in marine, ice and terrestrial archives, Clim. Past 7, 361–380. https://doi.org/10.5194/cp-7-361-2011.

Leonhardt, R., 2006. Analyzing rock magnetic measurements: The RockMagAnalyzer 1.0 software. Comput. Geosci. 32, 1420–1431. https://doi.org/10.1016/j.cageo.2006.01.006

Lisiecki, L.E., Raymo, M.E. 2005. A Pliocene-Pleistocene stack of 57 globally distributed benthic delta O-18 records. Paleoceanography 20, PA1003. https://doi.org/10.1029/2004PA001071

Liu, C., Deng, C., Liu, Q., 2012b. Mineral magnetic studies of the vermiculated red soils in southeast China and their paleoclimatic significance. Palaeogeogr., Palaeoclimatol., Palaeoecol. 329-330, 173–183. https://doi.org/10.1016/j.palaeo.2012.02.035

Liu, Q., Barrón, V., Torrent, J., Qin, H., Yu, Y., 2010. The magnetism of micro-sized hematite explained. Phys. Earth Planet. Int. 183 (3–4), 387–397. https://doi.org/10.1016/j.pepi.2010.08.008

Liu, Q., Deng, C., Torrent, J., Zhu, R., 2007. Review of recent developments in mineral magnetism of the Chinese loess. Quat. Sci. Rev. 26 (3–4), 368–385. https://doi.org/10.1016/j.quascirev.2006.08.004

Liu, Q., Jackson, M.J., Banerjee, S.K., Maher, B.A., Deng, C., Pan, Y., Zhu, R., 2004. Mechanism of the magnetic susceptibility enhancements of the Chinese loess. J. Geophys. Res. Solid Earth 109, 1–16. https://doi.org/10.1029/2004JB003249

Liu, Q., Roberts, A.P., Larrasoaña, J.C., Banerjee, S.K., Guyodo, Y., Tauxe, L. and Oldfield, F., 2012a. Environmental Magnetism: Principles and Applications. Rev. Geophys. 50, RG4002. https://doi.org/8755-1209/12/2012RG000393

Liu, Q., Zhang, C., Torrent, J., Barrón, V., Hu, P., Jiang, Z., Duan, Z., 2016. Factors controlling magnetism of reddish brown soil profiles from calcarenites in Southern Spain: dust input or in-situ pedogenesis? Front. Earth Sci., 4–51. https://doi.org/10.3389/feart.2016.00051

Long, X., Ji, J., Balsam, W., 2011. Rainfall-dependent transformations of iron oxides in a tropical saprolite transect of Hainan Island, South China: Spectral and magnetic measurements. J. Geophys. Res. Earth Surf. 116. doi:10.1029/2010JF001712

Long, X., Ji, J., Balsam, W., Barrón, V., Torrent, J., 2015. Grain growth and transformation of pedogenic magnetic particles in red Ferralsols. Geophys. Res. Lett. 42, 5762–5770. https://doi.org/10.1002/2015GL064678

Long, X., Ji, J., Barrón, V., 2016. Climatic thresholds for pedogenic iron oxides under aerobic conditions: Processes and their significance in paleoclimate reconstruction. Quat. Sci. Rev. 150, 264–277. https://doi.org/10.1016/j.quascirev.2016.08.031

Lorenzo, C., Carbonell, E., 1999. Representación espacial de los suelos de ocupación del nivel TG11 de Trinchera Galería, Sierra de Atapuerca, Burgos, in: Carbonell, E., Rosas, A., Díez, J.C. (Eds.), Atapuerca: Ocupaciones humanas y Paleoecología del yacimiento de Galería. Arqueología en Castilla y León, Junta de Castilla y León, Memorias 7, 79–94.

Lowrie, W., 1990. Identification of ferromagnetic minerals in a rock by coercivity and unblocking temperature properties. Geophys. Res. Lett., 17, 159–162. https://doi.org/10.1029/GL017i002p00159

Maher, B.,1986. Characterisation of soils by mineral magnetic measurements. Phys. Earth Planet. Int. 42 (1–2), 76–92. https://doi.org/10.1016/S0031-9201(86)80010-3

Maher, B.A., 1988. Magnetic properties of sorne synthetic sub-micron magnetites. Geophys. J., 94, 83–96. https://doi.org/10.1111/j.1365-246X.1988.tb03429.x

Maher, B.A., 1998. Magnetic properties of modern soils and quaternary loessic paleosols: Paleoclimatic implications. Palaeogeogr. Palaeoclimatol. Palaeoecol. 137 (1–2), 25–54. https://doi.org/10.1016/S0031-0182(97)00103-X

Maher, B., Taylor, R., 1988. Formation of ultrafine-grained magnetite in soils. Nature 336, 368–370. https://doi.org/10.1038/336368a0

Maher, B.A., Alekseev, A., Alekseeva, T., 2002. Variation of soil magnetism across the Russian steppe: Its significance for use of soil magnetism as a palaeorainfall proxy. Quat. Sci. Rev. 21, 1571–1576. https://doi.org/10.1016/S0277-3791(02)00022-7

Maher, B.A., Karloukovski, V.V., Mutch, T.J., 2004. High-field remanence properties of synthetic and natural submicrometre haematites and goethites: significance for environmental contexts. Earth Planet. Sci. Lett. 226, 491–505. https://doi.org/10.1016/j.epsl.2004.05.042

Maher, B.A., Possolo, A., 2013. Statistical models for use of palaeosol magnetic properties as proxies of palaeorainfall. Glob. Planet. Change 111, 280–287. doi:10.1016/j.gloplacha.2013.09.017

Maher, B.A., Thompson, R., 1999. Quaternary Climates, Environments and Magnetism, Cambridge University Press, 390 p.

Maher, B.A., Thompson, R., Zhou, L.P., 1994. Spatial and temporal reconstructions of changes in the Asian palaeomonsoon: A new mineral magnetic approach. Earth Planet. Sci. Lett. 125, 461–471. https://doi.org/10.1016/0012-821X(94)90232-1

Márton, E., Márton, P., Heller, F., 1980. Remanent magnetization of a Pliensbachian limestone sequence at Bakonycsernye (Hungary). Earth Planet. Sci. Lett. 48, 218–226. https://doi.org/10.1016/0012-821X(80)90183-1

Maxbauer, D.P., Feinberg, J.M., Fox, D.L., 2016a. MAX UnMix: A web application for unmixing magnetic coercivity distributions. Comput. Geosci. 95, 140–145. https://doi.org/10.1016/j.cageo.2016.07.009

Maxbauer, D.P., Feinberg, J.M., Fox, D.L., 2016b. Magnetic mineral assemblages in soils and paleosols as the basis for paleoprecipitation proxies: A review of magnetic methods and challenges. Earth Sci. Rev. 155, 28–48. https://doi.org/10.1016/j.epsl.2013.03.034

Melles, M., Brigham-Grette, J., Minyuk, P.S., Nowaczyk, N.R., Wennrich, V., DeConto, R.M., Anderson, P.M., Andreev, A.A., Coletti, A., Cook, T.L., Haltia-Hovi, E., Kukkonen, M., Lozhkin, A.V., Rosén, P., Tarasov, P., Vogel, H., Wagner, B. 2012. 2.8 Million Years of Arctic Climate Change from Lake El'gygytgyn, NE Russia. Science 337(6092), 315–320, https://doi.org/10.1126/science.1222135.

Moreno, J.M., 2005. A Preliminary General Assessment of the Impacts in Spain Due to the Effects of Climate Change. Ministerio Medio Ambiente, Univ. Castilla la Mancha, 786.

Mosquera, M., Ollé, A., Rodríguez, X.P., 2013. From Atapuerca to Europe: Tracing the earliest peopling of Europe. Quat. Int. 295, 130–137. doi:10.1016/j.quaint.2012.01.031

Ollé, A., Mosquera, M., Rodríguez, X.P., Lombera-Hermida, A., García-Antón, M.D., Garía-Medrano, P., Peña, L., Menéndez, L., Navazo, M., Terradillos, M., Bargalló, A., Márquez, B., Sala, R., Carbonell, E., 2013. The Early and Middle Pleistocene technological record from Sierra de Atapuerca (Burgos, Spain). Quat. Int. 295, 138–167. https://doi.org/10.1016/j.quaint.2011.11.009

Ortega, A.I., 2009. La evolución geomorfológica del karst de la Sierra de Atapuerca (Burgos) y su relación con los yacimientos pleistocenos que contiene. Ph.D. thesis, University of Burgos, Spain.

Ortega, A.I., Benito-Calvo, A., Pérez-González, A., Carbonell, E., Bermúdez de Castro, J. M., Arsuaga, J. L., 2014. Atapuerca karst and its paleoanthropological sites, in: Gutiérrez, F., Gutiérrez M. (Eds.), Landscapes and Landforms of Spain, World Geomorphological Landscapes, Springer Science+Business Media Dordrecht, pp. 101–110. https://doi.org/10.1007/978-94-017-8628-7_8

Ortega, A.I., Benito-Calvo, A., Pérez-González, A., Martín-Merino, M.A., Pérez-Martínez, R., Parés, J.M., Aramburu, A., Arsuaga, J.L., Bermúdez de Castro, J.M., Carbonell, E., 2013. Evolution of multilevel caves in the Sierra de Atapuerca (Burgos, Spain) and its relation to human occupation. Geomorphology 196, 122–137. https://doi.org/10.1016/j.geomorph.2012.05.031

Özdemir, Ö., Banerjee, S.K., 1984. High temperature stability of magnetite (γ-Fe_2O_3). Geophys. Res. Lett., 11(3), 161–164. https://doi.org/10.1029/GL011i003p00161

Palmer, A., 2005. Inceptisols, in: Hillel, D. (Ed). Encyclopedia of Soils in the Environment, Elsevier, pp. 248–254, ISBN 9780123485304, https://doi.org/10.1016/B0-12-348530-4/00027-8.

Panaiotu, C.G., Panaiotu, E.C., Grama, A., Necula, C., 2001. Paleoclimatic record from a loess-paleosol profile in Southeastern Romania. Phys. Chem. Earth, Part A Solid Earth Geod. 26, 893–898. https://doi.org/10.1016/S1464-1895(01)00138-7

Parés, J. M., Pérez-González, A., 1999. Magnetochronology and stratigraphy at Gran Dolina section, Atapuerca (Burgos, Spain). J. Hum. Evol. 37, 325–342. https://doi.org/10.1006/jhev.1999.0331

Parés, J.M., Pérez-González, A., Arsuaga, J.L., Bermúdez De Castro, J.M., Carbonell, E., Ortega, A.I., 2010. Characterizing the sedimentary history of cave deposits, using archaeomagnetism and rock magnetism, Atapuerca (Northern Spain). Archaeometry 52, 882–898. https://doi.org/10.1111/j.1475-4754.2010.00533.x

Parés, J.M., Pérez-González, A., 1995. Paleomagnetic age for hominid fossils at Atapuerca Archaeological Site, Spain. Science 269, 830–832. https://doi.org/10.1126/science.7638599

Parés, J.M., Pérez-González, A., Rosas, A., Benito, A., Bermúdez de Castro, J.M., Carbonell, E., Huguet, R., 2006. Matuyama-age lithic tools from the Sima del Elefante site, Atapuerca (northern Spain), J. Hum. Evol., 50 (2), 163–169. https://doi.org/10.1016/j.jhevol.2005.08.011

Parés, J.M., Pérez-González, A., Weil, A.B., Arsuaga, J.L., 2000. On the age of the hominid fossils at the Sima de los Huesos, Sierra de Atapuerca, Spain: paleomagnetic evidence. Am. J. Phys. Anthropol. 111, 451–461. http://hdl.handle.net/2027.42/34269

Past Interglacials Working Group of PAGES, 2016. Interglacials of the last 800,000 years. Rev. Geophys. 54, 162–219, https://doi.org/10.1002/2015RG000482.

Peel, M.C., Finlayson, B.L., McMahon, T.A., 2007. Updated world map of the Köppen-Geiger climate classification. Hydrol. Earth Syst. Sci. 11, 1633–1644. https://doi.org/10.5194/hess-11-1633-2007

Pennos, C., Aidona, E., Pechlivanidou, S., Vouvalidis, K., 2014. Holocene sedimentary records of the katarraktes cave system (Northern Greece): A stratigraphical and environmental magnetism approach. Acta Carstologica 43, 43–54. https://doi.org/10.3986/ac.v43i1.627

Pérez-González, A., Aleixandre, T., Pinilla, A., Gallardo, J., Benayas, J., Martínez, M.J., Ortega, A.I., 1995. Aproximación a la estratigrafía de Galería en la trinchera de Atapuerca (Burgos), in: Bermúdez de Castro, J.M., Arsuaga, J.L., Carbonell, E., (Eds.), Evolución humana en Europa y los yacimientos de la Sierra de Atapuerca, Junta de Castilla y León, pp. 99–122.

Pérez-González, A., Parés, J.M., Carbonell, E., Aleixandre, T., Ortega, A.I., Benito, A., Martín Merino, M.A., 2001. Géologie de la Sierra de Atapuerca et stratigraphie des remplissages karstiques de Galería et Dolina (Burgos, Espagne). L'Anthropologie, 105, 27–43. https://doi.org/10.1016/S0003-5521(01)80004-2

Pérez-González, A., Parés, J.M., Gallardo, J., Aleixandre, T., Ortega, A.I., Pinilla, A., 1999. Geología y estratigrafía del relleno de Galería de la Sierra de Atapuerca (Burgos), in: Carbonell, E., Rosas, A., Díez, J.C., (Eds.), Atapuerca: Ocupaciones humanas y paleoecología del yacimiento de Galería, Arqueología en Castilla y León, Junta de Castilla y León, Memorias 7, pp. 31–42

Peters, C., Dekkers, M. J., 2003. Selected room temperature magnetic parameters as a function of mineralogy, concentration and grain size. Phys. Chem. Earth 28 (16–19), 659–667. https://doi.org/10.1016/S1474-7065(03)00120-7

Pospelova, G., Król, E., Levkovskaya, G., Kruczyk, J., Kądziałko-Hofmokl, M., Kulakov, S., 2007. Magnetic, paleomagnetic and palynologic studies of Paleolithic depositions of the Akhshtyrskaya cave (Russia). Acta Geophys. 55, 619–639. https://doi.org/10.2478/s11600-007-0019-1

Prokopenko, A.A., Hinnov, L.A. Williams, D.F., Kuzmin, M.I. 2006. Orbital forcing of continental climate during the Pleistocene: A complete astronomically tuned climatic record from Lake Baikal, SE Siberia, Quat. Sci. Rev., 25(23–24), 3431–3457, https://doi.org/10.1016/j.quascirev.2006.10.002.

Pruner, P., Hajna, N.Z., Mihevc, A., Bosák, P., Man, O.P.S., Venhodová, D., 2010. Magnetostratigraphy and fold tests from Raciska Pecina and Pecina V Borstu caves (classical karst, Slovenia). Stud. Geophys. Geod. 54, 27–48. https://doi.org/10.1007/s11200-010-0002-1

Robertson, D.J., France, D.E., 1994. Discrimination of remanence-carrying minerals in mixtures, using isothermal remanent magnetisation acquisition curves. Phys. Earth Planet. Inter. 82, 223–234. https://doi.org/10.1016/0031-9201(94)90074-4

Roberts, A.P., Yulong Cui, Verosub, K.L., 1995. Wasp-waisted hysteresis loops: mineral magnetic characteristics and discrimination of components in mixed magnetic systems. J. Geophys. Res. 100, 17909–17924. https://doi.org/10.1029/95jb00672

Roberts, A.P., Zhao, X., Heslop, D., Abrajevitch, A., Chen, Y.H., Hu, P., Jiang, Z., Liu, Q., Pillans, B.J., 2020. Hematite (α-Fe_2O_3) quantification in sedimentary magnetism: limitations of existing proxies and ways forward. Geosci. Lett. 7:8. doi:10.1186/s40562-020-00157-5

Rodríguez, J., Burjachs, F., Cuenca-Bescós, G., García, N., Van der Made, J., Pérez González, A., Blain, H.A., Expósito, I., López-García, J.M., García Antón, M., Allué, E., Cáceres, I., Huguet, R., Mosquera, M., Ollé, A., Rosell, J., Parés, J.M., Rodríguez, X.P., Díez, C., Rofes, J., Sala, R., Saladié, P., Vallverdú, J., Bennasar, M.L., Blasco, R., Bermúdez de Castro, J.M., Carbonell, E., 2011. One million years of cultural evolution in a stable environment at Atapuerca (Burgos, Spain). Quat. Sci. Rev. 30, 1396–1412. https://doi.org/10.1016/j.quascirev.2010.02.021

Rosas, A., Carbonell, E., Cuenca, G., García, N., Fernández Jalvo, Y, van der Made, J., Ollé, A., Parés, J.M., Pérez-González, A., Sánchez Marco, A., Sánchez Chillón, B., Vallverdú, J., 1998. Cronología, bioestratigrafía y paleoecología del Pleistoceno Medio de Galería (Sierra de Atapuerca, España). Revista Española de Paleontología 13, 71–80.

Rosas, A., Bermúdez de Castro, J.M., 1999. Descripción y posición evolutiva de la mandíbula AT76-T1H del yacimiento de Galería (Sierra de Atapuerca), in: Carbonell, E., Rosas, A., Díez, J.C, (Eds.), Atapuerca: Ocupaciones humanas y paleoecología del yacimiento de Galería, Arqueología en Castilla y León, Junta de Castilla y León, Memorias 7, pp. 237–243.

Roucoux, K.H., Tzedakis, P.C., de Abreu, L., Shackleton, N.J., 2006. Climate and vegetation changes 180,000 to 345,000 years ago recorded in a deep-sea core off Portugal. Earth Planet. Sci. Lett. 249, 307–325. doi:10.1016/j.epsl.2006.07.005

Schwertmann, U., 1971. Transformation of hematite to goethite in soils. Nature 232 (5313), 624–625. https://doi.org/10.1038/232624a0

Schwertmann, U., 1988. Occurrence and formation of iron oxides in various pedoenvironments, in: Stucki, J.W, Goodman, B.A., Schwertmann, U., (Eds.), Iron in Soils and Clay Minerals, Reidel Publishing, pp. 267-308.

Sroubek, P., 2007. Paleoenvironmental reconstructions from cave sediments of the Moravian Karst, PhD Thesis, Czech Republic.

Suganuma Y., Okada M., Horie K., Kaiden H., Takehara M., Senda R., Kimura J.-I., Kawamura K., Haneda Y., Kazaoka O. and Head M. J. (2015) Age of Matuyama-Brunhes boundary constrained by U–Pb zircon dating of a widespread tephra. Geology 43, 491–494. https://doi.org/10.1130/G36625.1

Temovski, M., Pruner, P., Hercman, H., Bosák, P., 2016. A cave response to environmental changes in the Late Pleistocene: a study of Budimirica Cave sediments, Macedonia. Geol. Croat. 69, 307–316. https://doi.org/10.4154/gc.2016.29

Torrent, J., Barrón, V., Liu, Q., 2006. Magnetic enhancement is linked to and precedes hematite formation in aerobic soil. Geophys. Res. Lett. 33 (2), 4–7. https://doi.org/10.1029/2005GL024818

Torrent, J., Liu, Q.-S., Bloemendal, J., Barron, V., 2007. Magnetic enhancement and iron oxides in the upper Luochuan loess–paleosol sequence, Chinese Loess Plateau. Soil Sci. Soc. Am. J. 71, 1570–1578. doi:10.2136/sssaj2006.0328

Torrent, J., Liu, Q.S., Barrón, V., 2010a. Magnetic susceptibility changes in relation to pedogenesis in a Xeralf chronosequence in northwestern Spain. European Journal of Soil Science 61 (2), 161–173. https://doi.org/10.1111/j.1365-2389.2009.01216.x

Torrent, J., Liu, Q.S., Barrón, V., 2010b. Magnetic minerals in Calcic Luvisols (Chromic) developed in a warm Mediterranean region of Spain: Origin and paleoenvironmental significance. Geoderma, 154 (3–4), 465–472. https://doi.org/10.1016/j.geoderma.2008.06.020

Tzedakis, P. C., Hooghiemstra, H., Palike, H. 2006. The last 1.35 million years at Tenaghi Philippon: Revised chronostratigraphy and long-term vegetation trends. Quat. Sci. Rev., 25(23–24), 3416–3430. https://doi.org/10.1016/j.quascirev.2006.09.002

Vallverdú i Poch, J., 2017. Soil-stratigraphy in the cave entrance deposits of Middle Pleistocene age at the Trinchera del Ferrocarril sites (Sierra de Atapuerca, Spain). Quat. Int. 433, 199–210. https://doi.org/10.1016/j.quaint.2015.09.031

Vallverdú, J., 1999. Microfacies y Micromorfología de las Unidades G.II y G.III de Galería (Sierra de Atapuerca), in: Carbonell, E., Rosas, A., Díez, J.C., (Eds.), Atapuerca: Ocupaciones humanas y paleoecología del yacimiento de Galería, Arqueología en Castilla y León, Junta de Castilla y León, Memorias 7, pp. 43–54.

Vicente-Serrano, S.M., Rodríguez-Camino, E., Domínguez-Castro, F., El Kenawy, A., Azorín-Molina, C., 2017. An updated review on recent trends in observational surface atmospheric variables and their extremes over Spain. Cuad. Investig. Geogr. 43, 209–232. https://doi.org/10.18172/cig.3134

Wang, K., Dickinson, R., 2012. A review of global terrestrial evapotranspiration: observation, modeling, climatology, and climatic variability. Rev. Geophys. 50, 1–54. https://doi.org/10.1029/2011RG000373

Warrier, A.K., Sandeep, K., Harshavardhana, B.G., Shankar, R., Pappu, S., Akhilesh, K., Prabhu, C.N., Gunnell, Y., 2011. A rock magnetic record of Pleistocene rainfall variations at the Palaeolithic site of Attirampakkam, Southeastern India. J. Archaeol. Sci. 38, 3681–3693. https://doi.org/10.1016/j.jas.2011.08.039

Zhao, L., Hong, H., Fang, Q., Yin, K., Wang, C., Li, Z., Torrent, J., Cheng, F., Algeo, T.J., 2017. Monsoonal climate evolution in southern China since 1.2 Ma: New constraints from Fe-oxide records in red earth sediments from the Shengli section, Chengdu Basin. Palaeogeogr. Palaeoclimatol. Palaeoecol. 473, 1–15. https://doi.org/10.1016/j.palaeo.2017.02.027